UNIVERSITY OF OKLAHOMA

GRADUATE COLLEGE

PROCESS DEVELOPMENT FOR HIAM OF CERIA-STABILIZED ZIRCONIA: LINKING HYDROGEL NETWORK CHARACTERISTICS TO CE/ZR INFUSION AND 3D LATTICE FABRICATION

A THESIS
SUBMITTED TO THE GRADUATE FACULTY
in partial fulfillment of the requirements for the
Degree of
MASTER OF SCIENCE

By PETER KWASI SARPONG AMPRAKO
Norman, Oklahoma
2026

PROCESS DEVELOPMENT FOR HIAM OF CERIA-STABILIZED ZIRCONIA: LINKING HYDROGEL NETWORK CHARACTERISTICS TO CE/ZR INFUSION AND 3D LATTICE FABRICATION

A THESIS APPROVED FOR THE

SCHOOL OF AEROSPACE AND MECHANICAL ENGINEERING

BY THE COMMITTEE CONSISTING OF

Dr. Shuozhi Xu, Chair

Dr. Jingyao Dai, Co-chair

Dr. Iman Ghamarian

Acknowledgements

First and foremost, I give all glory and honor to God Almighty, whose goodness and mercies have carried me every step of this journey. It is by His grace alone that I have come this far.

I am deeply grateful to my primary advisor, Dr. Shuozhi Xu, for his guidance, patience, and intellectual generosity throughout this research. His mentorship has shaped not only this work but my growth as a researcher. I am equally thankful to my secondary advisor, Dr. Jingyao Dai, for his support and the invaluable perspective he brought to this project. I would also like to extend sincere appreciation to Dr. Iman Ghamarian for his encouragement and technical insight at critical moments in this work and my journey overall at the University of Oklahoma.

This thesis would not have been possible without the support of two exceptional research communities. To the members of the Computational Materials, Mechanics, and Manufacturing Laboratory (CM3 Lab) and the Nanostructured Aerospace Materials Laboratory (NAML), thank you for the stimulating discussions, the shared challenges, and the camaraderie that made this experience meaningful.

A special word of thanks goes to Jiehua Li and Isabella Jensen, who spent countless hours with me in the lab. Your dedication and friendship made the hardest days manageable.

I owe a profound debt of gratitude to the Shelby Davis Foundation and the United World College, whose scholarship made it possible for me to pursue the International Baccalaureate and whose generosity extended further still in funding my undergraduate education at the University of Oklahoma. That investment changed the trajectory of my life, and I carry it with me in everything I do.

I would also like to thank the Ronnie K. Irani Center for the Creation of Economic Wealth (ICCEW) for granting me a Graduate Assistantship at a moment when the path forward was uncertain. The opportunity to serve as a fellow on the product design team gave me far more than financial support. The mentorship I received there taught me perseverance that carried me through the most difficult stretches of this work. To my colleagues and supervisors at ICCEW, thank you for the conversations, for pouring into me, and for believing in what I could become, both as a professional and as a person.

My appreciation goes to the Kofa and Hodo families for being a home away from home and making me feel welcome whenever I was invited to their homes.

Finally, to my family and friends, your love, sacrifice, and unwavering belief in me have been my foundation. Words are not enough, but I hope this work is a testament to everything you have invested in me.

Dedication

To my nephew, Ephraim Papa Kofi Adom Amprako. ad astra per aspera

Table of Contents

Acknowledgements iv

Dedication v

Table of Figures ix

Table of Tables x

Abstract xii

Chapter 1 : Introduction 1

1.1 Hydrogel Infused Additive Manufacturing 3

1.2 Thesis Overview 6

Chapter 2 : Background and Literature Review 8

2.1 Additive Manufacturing of Ceria-Stabilized Zirconia 8
2.1.1 Powder-Based Additive Manufacturing of Ceramics 8
2.1.2 Resin-Based Additive Manufacturing of Ceramics 10
2.2 Hydrogel Infusion Additive Manufacturing (HIAM) 12
2.2.1 Principles and Process Overview 12
2.2.2 HIAM for Metal Oxide Systems 14
2.2.3 Limitations of HIAM and Recent Advances 17
2.3 Potential Challenges of HIAM for Ceria-Stabilized Zirconia 18
2.4 Motivation for the Present Study 20
Chapter 3 Chapter 3: Objectives and Approach 21
3.1 Research Goal 21
3.2 Hypotheses 21
3.3 Objectives 22
3.4 Approach 22
3.4.1 Parametric Study of Resin Composition 22
3.4.2 Infusion Behavior of Ce and Zr Salt Solutions 22
3.4.3 Fabrication of CSZ Lattice Structures 23

Chapter 4 : Effect of Resin Composition on Hydrogel Network Characteristics 23
4.1 Motivation 23
4.2 Design of Experiments 23
4.3 Materials and Methods 24
4.3.1 Mold Fabrication 25
4.3.2 Curing Procedure 25
4.3.3 Swelling and Water Content Characterization 26
4.4 Results 27
4.4.1 Effect of PEGDA/PEGMA Ratio 29
4.4.2 Effect of Starting Water Content 30
4.5 Discussion 31
Chapter 5 : Infusion Behavior of Cerium and Zirconium Precursors in HIAM 31
5.1 Introduction 31
5.2 Design of Experiments 32
5.3 Materials and Methods 33
5.3.1 Preparation of Salt Solutions 33
5.3.2 Infusion Procedure 33
5.4 Results 34
5.4.1 Room Temperature Infusion Behavior 34
5.4.2 Elevated Temperature Infusion Behavior 36
5.4.3 Implications for HIAM of Ceria-Stabilized Zirconia 39
5.5 Discussion 39
Chapter 6 : Demonstration of HIAM 3D printing of Zirconia-based Ceramic Lattices 41
6.1 Introduction 41
6.2. Materials and Methods 42
6.2.1 Resin Formulation 42
6.2.2 Lattice Design 42
6.2.3 Printing Parameters and Procedure 43
6.2.4 Infusion 46
6.2.5 Precipitation 47
6.3 Results 48
6.3.1 Printed Lattice Morphology 48

6.3.2 Mass Evolution Through the HIAM Process 48
6.4 Discussion 53
Chapter 7 Conclusions and Future Work 54
7.1 Summary of Results 54
7.2 Implications 54
7.3 Challenges and Limitations 56
7.4 Future Work 58
Chapter 8 References 61

Table of Figures

Figure 1-1:Classification of additive manufacturing processes by feedstock state (after Godec et al., 2021; ISO/ASTM 52900).....**Error! Bookmark not defined.**

Figure 1-2: Positioning of HIAM within the vat photopolymerization family of additive manufacturing processes 4

Figure 2-1: Schematic comparison of UV light propagation in a ceramic-loaded resin (left) versus a particle-free hybrid resin (right). Solid particles scatter and attenuate the beam, limiting resolution, while dissolved ions allow free propagation and high-resolution photopolymerization. 12

Figure 2-2: Schematic of the cross-section of a bottom-up LCD-DLP printer. UV light is patterned by the LCD and cured through the FEP film layer by layer, with the build plate rising to grow the part. 13

Figure 2-3: Schematic of the four-stage HIAM process: (1) vat photopolymerization of a particle-free hydrogel scaffold, (2) immersion in aqueous metal salt solution to infuse target cations into the polymer network, (3) precipitation to fix the metal ions within the hydrogel, and (4) calcination and sintering to burn off the polymer and densify the ceramic. 14

Figure 4-1: Mold fabrication approach for resin specimen casting 26

Figure 4-2: Specimen preparation procedure. (1) Resin formulations A, B, and C were pipetted into silicone molds. (2) Each filled mold was cured in a Phrozen UV cure unit at three exposure durations (10, 15, and 20 seconds) to assess the effect of curing time on hydrogel network formation. 25

Figure 4-3: Equilibrium Water Content as a Function of PEGDA/PEGMA Ratio and Initial Water Content (10 s UV Exposure) 27

Figure 4-4: Equilibrium Water Content as a Function of PEGDA/PEGMA Ratio and Initial Water Content (15 s UV Exposure) 28

Figure 4-5: Equilibrium Water Content as a Function of PEGDA/PEGMA Ratio and Initial Water Content (20 s UV Exposure) 28

Figure 5-1 Normalized mass change (%) during room temperature infusion for Ce and Zr salt systems. 34

Figure 5-2: Normalized mass change (%) during infusion at 60°C for Ce and Zr salt systems... 36

Figure 5-3: Normalized mass change (%) for all four infusion conditions across the measurement window. 38

Figure 6-1: — CAD rendering of the 10 x 10 x 10 mm gyroid lattice (2.5 mm unit cell) 43

Figure 6-2: Observed failure modes during DLP printing of PEGDA/PEGMA hydrogel gyroid lattices on the Phrozen Sonic Mini 8K 46

Figure 6-3: Photograph of gyroid lattice before infusion (clear/white) and after infusion (yellow-orange coloration from Ce3+ ions) 47

Figure 6-4: Gyroid lattice after the first (left) and second (right) ammonium vapor precipitation cycles 48

Figure 6-5: Photographs of the successful gyroid hydrogel structures 48

Table of Tables

Table 2-1: A comparison of powder-based AM techniques 9

Table 2-2: Summary of prior HIAM demonstrations, organized by generation. First-generation studies (Gen 1) used a single infusion-precipitation cycle and reported linear shrinkage of 60–90%. Second-generation work (Gen 2) by Ji and Yee employed ten sequential cycles, reducing shrinkage to approximately 20% for ceramics and 38% for metals. 15

Table 2-3: Precursor Solubility Comparison 18

Table 4-1: Experimental matrix for the parametric hydrogel formation study 24

Abstract

Hydrogel-infusion additive manufacturing (HIAM) is a vat photopolymerization-based technique that decouples geometry definition from material selection, using a particle-free hydrogel scaffold as a structural template into which material identity is introduced through post-print infusion of aqueous metal salt precursors. This thesis investigates the application of HIAM to the fabrication of ceria-stabilized zirconia (CSZ) ceramic lattices and establishes the link between hydrogel network characteristics, Ce/Zr infusion behavior, and 3D lattice fabricability. This material system presents distinct challenges relative to prior HIAM demonstrations due to the limited aqueous solubility of zirconium precursors and the differential interaction of Ce^{3+} and Zr^{4+} with the polymer network.

A 3×3 factorial parametric study varying PEGDA/PEGMA molar ratio (100/0, 75/25, 50/50) and polymer-to-water weight fraction (30/70, 50/50, 70/30) across three UV exposure durations (10, 15, 20 s) identified the network formulation that maximizes equilibrium water content (EWC). The highest EWC of 71.70% was achieved with 50/50 PEGDA/PEGMA, 30/70 polymer/water at 10 s UV exposure (Vial 7), representing an improved composition for ion infusion. However, Vial 7 could not be reliably printed on the Phrozen Sonic Mini 8K due to its high water content, and the next-best formulation (Vial 8: 50/50 PEGDA/PEGMA, 50/50 polymer/water, 10 s UV) was adopted as the working formulation for all subsequent printing and infusion work.

Infusion experiments with 2 M $CeCl_3 \cdot 7H_2O$ and 2 M $ZrOCl_2 \cdot 8H_2O$ solutions revealed an asymmetry in ion uptake. Ce^{3+}-infused discs achieved a net overnight mass gain of approximately 11.4% above the swollen baseline, while Zr^{4+}-infused discs reached only approximately 6.7%, consistent with the higher charge density and reduced mobility of Zr^{4+} within the polymer network. Elevated-temperature infusion at 60 °C accelerated kinetics but

introduced concave warping incompatible with geometric fidelity, identifying room-temperature overnight infusion at 2 M as the most suitable condition. Preliminary precipitation trials using ammonium hydroxide solution were unsuccessful, as the precipitating agent displaced previously absorbed ions rather than fixing them within the network.

Gyroid lattice structures were printed using the Vial 8 formulation and advanced to the precipitation stage, with two surviving structures obtained from approximately 24 attempts due to build plate adhesion failures and the geometric demands of the gyroid architecture. The results establish an initial process window for CSZ HIAM and identify three technical barriers that must be addressed to advance the material system toward functional ceramic fabrication: precursor loading, precipitation chemistry, and print process reliability.

Chapter 1 : Introduction

Additive manufacturing (AM), commonly referred to as 3D printing, constructs objects by building up material, often layer by layer, directly from a digital model. It is called additive because, unlike traditional subtractive manufacturing, which begins with stock material and removes unwanted portions until the desired shape remains, AM deposits material only where it is needed until the complete part is formed. This fundamental distinction enables structural and functional designs that are difficult or impossible to achieve through conventional fabrication. Complex internal architectures such as lattice cores and mechanical metamaterials can be precisely engineered to tailor stiffness, strength, damping, and thermal properties. AM also supports the fabrication of functionally graded and multi-material parts, where composition or microstructure varies spatially to meet localized loading, weight, or thermal requirements. Through topology optimization and controlled porosity, components can be made significantly lighter without sacrificing structural performance. Beyond the final part itself, AM accelerates the design-to-test cycle by enabling rapid prototyping, reducing both development time and cost. Additive manufacturing methods can be broadly categorized according to their feedstock state and energy source, as illustrated in Figure 1-1[1].

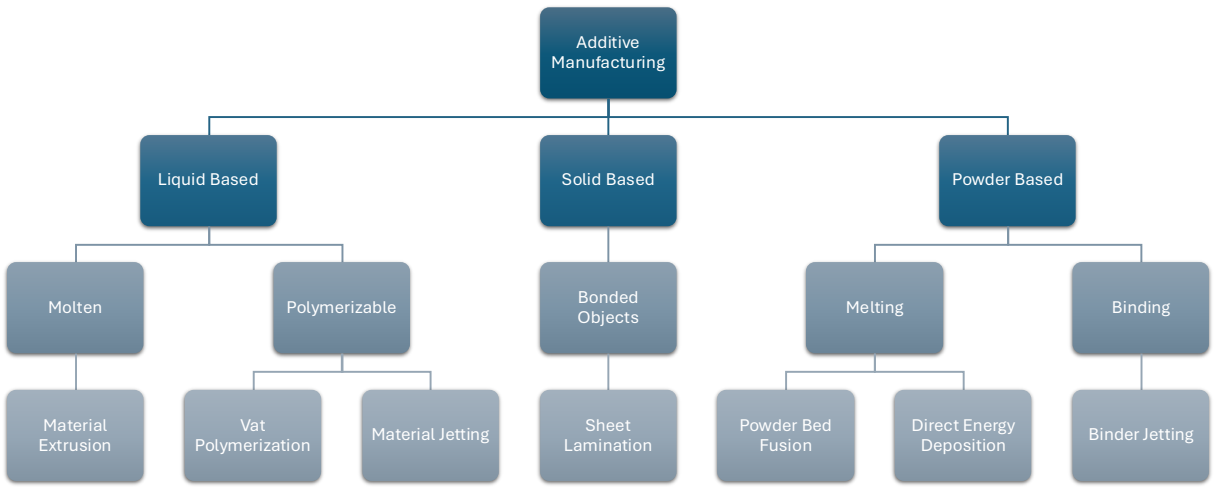

Figure 1-1: Classification of additive manufacturing processes by feedstock state (after Godec et al., 2021; ISO/ASTM 52900)

In powder bed fusion (PBF), a focused energy source, either a laser in selective laser melting (SLM) or an electron beam in electron beam melting (EBM), selectively consolidates metal or ceramic powders layer by layer [2]. Binder jetting follows a similar powder bed approach but uses a liquid binder to bond powder particles, with the green part subsequently densified through sintering or infiltration [3]. Material extrusion encompasses fused deposition modeling (FDM) for thermoplastic filaments and direct ink writing (DIW) for paste-like ceramic or metal-loaded inks, while directed energy deposition (DED) is a distinct process category in which a focused energy source melts blown powder or wire feedstocks simultaneously with deposition.[4],[5],[6]. Vat photopolymerization processes, including stereolithography (SLA) and digital light processing (DLP), cure liquid polymer resins using ultraviolet or visible light, and can be extended to ceramic or preceramic systems through particle-loaded resins [7],[8]. Droplet-based methods such as material jetting, aerosol jetting, and inkjet printing deposit polymers, ceramics, or functional suspensions with high spatial precision [9],[10]. Finally, a range of other paradigms including electrochemical deposition, and various hybrid approaches offer additional flexibility for specialized material systems and applications [11].

Among these, ceramic additive manufacturing has attracted growing interest and represents an active frontier. Current state-of-the-art approaches fall broadly into two categories: powder-based methods, in which a green body is formed layer by layer and subsequently densified through calcination and sintering, and resin-based methods, in which photopolymerizable resins loaded with ceramic particles or preceramic polymers are cured via SLA or DLP and then pyrolyzed and sintered to yield the final ceramic part. Despite their differences in feedstock and processing, both approaches share a common challenge. The thermal post-processing steps involve significant binder burnout and densification, leading to high mass loss and substantial volumetric shrinkage. If not carefully controlled, this shrinkage can be anisotropic and non-uniform, resulting in warping, cracking, and reduced geometric fidelity [12]. Addressing these limitations remains a key barrier to the broader adoption of ceramic AM for precision applications.

1.1 Hydrogel Infused Additive Manufacturing

Hydrogel-infused additive manufacturing, or HIAM, is a vat photopolymerization-based technique that decouples the two decisions that conventional ceramic AM forces simultaneously: what shape to print, and what material to print it in [13]. In traditional ceramic AM, the feedstock resin or slurry is formulated for a specific target material from the outset, meaning a change in material requires a redesigned resin, re-optimized print parameters, and a fresh round of process development [13]. HIAM sidesteps this entirely by using a single, material-agnostic hydrogel scaffold as the structural template, with material identity introduced only after the scaffold has been printed [13], [14].

Figure 1-2 shows how HIAM is positioned within the vat photopolymerization family of AM processes, contrasted with the two alternative resin-based approaches it was developed to overcome.

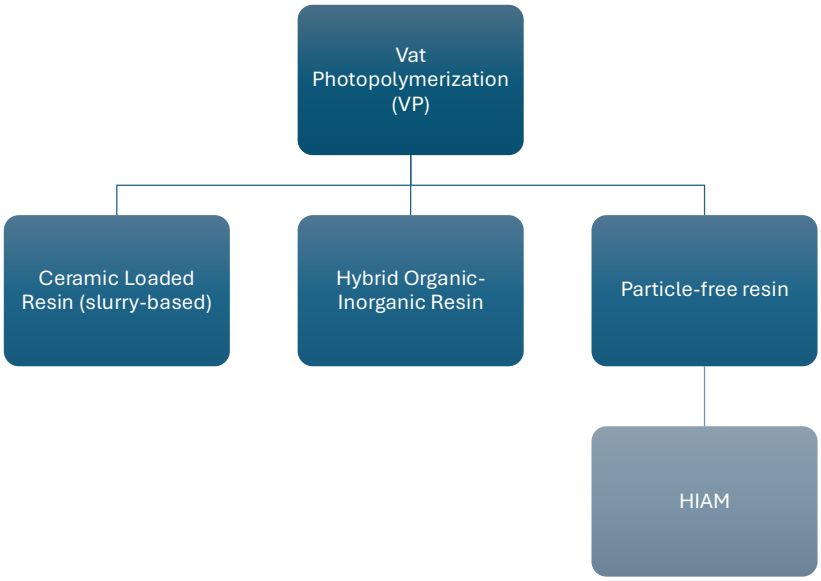

Figure 1-2: Positioning of HIAM within the vat photopolymerization family of additive manufacturing processes

The HIAM process begins with vat photopolymerization of an organogel(hydrogel), typically a DMF/PEGDA-based resin, into the desired three-dimensional architecture [13]. This printed organogel is then converted into a hydrogel replica through solvent exchange in water, yielding a dimensionally accurate, polymer network. The hydrogel is subsequently immersed in an aqueous salt solution, allowing target cations to diffuse into and throughout the polymer network. Thermal treatment in air through calcination burns away the polymer scaffold and converts the infused metal ions to their oxide forms[15]. Where a pure metal or alloy is desired rather than an oxide, a further reduction step in forming gas completes the conversion, leaving behind a high-resolution metallic replica of the original printed geometry. This is shown in Figure 1-3 below.

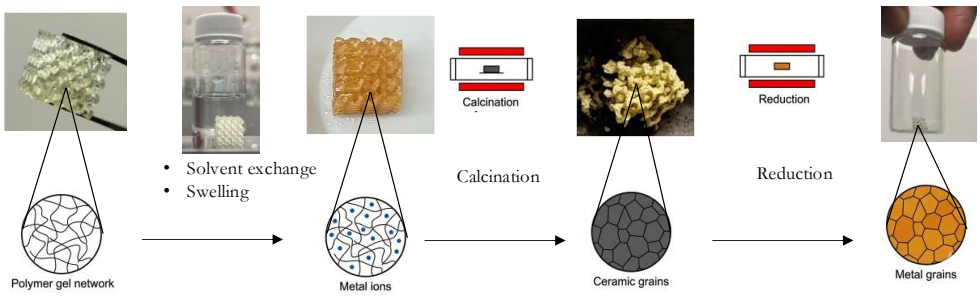

Figure 1-3: Showing a description of how Hydrogel Infused AM works

The most significant advantage of this approach is the temporal separation of geometry definition and material selection. Because the scaffold is printed from a transparent, particle-free resin, it avoids the light-scattering that limits resolution in slurry-based systems and can achieve feature sizes down to approximately 250 nm for metal oxide structures , well beyond what particle-loaded resins can reliably produce [15]. The resin chemistry is also substantially simpler, eliminating the need to engineer slurry rheology, particle dispersion stability, or inorganic-organic hybrid precursors for every new target material.

That said, HIAM is not without its challenges. As a technique still in early development, with second-generation methods only emerging in 2024 and 2025, the process window and failure modes are not yet fully mapped. Different metal cations interact with the PEG backbone in fundamentally different ways: trivalent ions such as Fe^{3+} coordinate more strongly with the polymer than divalent ions, which complicates achieving precise target stoichiometries in multi-component systems. Most practically, the conversion process involves substantial mass loss and volumetric shrinkage. Linear shrinkage of 60 to 90% was common in early implementations, which, if not carefully managed, manifests as internal voids, cracking, and loss of geometric fidelity [16]. Controlling and ultimately reducing this shrinkage is one of the central engineering challenges the field is currently working to address.

1.2 Thesis Overview

This thesis investigates the application of hydrogel-infused additive manufacturing to the fabrication of ceria-stabilized zirconia (CSZ) ceramic lattices, with the goal of establishing a reliable process for HIAM of zirconia-based ceramics while maximizing metal ion loading to limit volumetric shrinkage.

Chapter 2 provides a background and literature review covering prior additive manufacturing studies for ceria-stabilized zirconia, including both powder-based and resin-based approaches. It then offers a more detailed treatment of HIAM, reviewing prior demonstrations across metal and ceramic material systems, the limitations identified in those studies, and the specific challenges anticipated for applying HIAM to CSZ.

Subsequently, chapter 3 defines the objectives and approach of the study. It states the central hypotheses guiding the experimental design and outlines the three primary objectives: characterizing how resin composition affects hydrogel network properties, studying the infusion behavior of cerium and zirconium precursors, and demonstrating HIAM fabrication of CSZ lattices.

Then chapter 4 presents a parametric study examining how PEGDA/PEGMA ratio and initial water content influence the physical characteristics of the swelled hydrogel network, including swollen water fraction and polymer mesh size. The results of this study inform the selection of the resin formulation used in subsequent chapters.

Chapter 5 investigates the infusion behavior of cerium salt, zirconium salt, and their mixture in the hydrogel selected in Chapter 4. Weight change measurements and structural observations are used to assess infusion kinetics, ion uptake capacity, and the feasibility of multi-stage infusion-precipitation as a strategy for increasing ceramic yield.

Chapter 6 applies the knowledge developed in Chapters 4 and 5 to demonstrate the HIAM fabrication of zirconia-based ceramic lattices.

Chapter 7 summarizes the key findings of the study, discusses their implications for the broader development of HIAM as a ceramic fabrication platform, and identifies directions for future work.

Chapter 2 : Background and Literature Review

2.1 Additive Manufacturing of Ceria-Stabilized Zirconia

Prior research into the additive manufacturing (AM) of ceria-stabilized zirconia (Ce-ZrO_2, commonly Ce-TZP) has been motivated by this material's superior fracture toughness of approximately 11 $MPa \cdot m^{\frac{1}{2}}$ and its exceptional resistance to low-temperature degradation (hydrothermal aging) relative to the more widely studied yttria-stabilized zirconia (Y-TZP) [17]; [18]. The stabilization of the zirconia tetragonal phase by cerium oxide enables a stress-induced martensitic transformation toughening mechanism at crack tips, which makes Ce-TZP particularly attractive for structural and biomedical applications where cyclic loading and aqueous environments are present [13]. Despite these advantages, the AM of Ce-TZP remains significantly less developed than that of Y-TZP, and the existing body of work can be broadly categorized into powder-based and resin-based approaches. Zirconium dioxide (ZrO2) was discovered accidentally by German chemist Martin H. Klaproth in 1789 during his work on gemstones. It was only in the 1960 that more work was done to learn about the uses of zirconium especially its use as a biomaterial. In 1969, it was used in the medical field as material for hip head replacement instead of titanium or alumina prostheses [19].

2.1.1 Powder-Based Additive Manufacturing of Ceramics

Powder-based AM techniques encompass a range of methods including Selective Laser Sintering (SLS), Selective Laser Melting (SLM), and Binder Jetting (BJ). In SLS and SLM, a high-power laser selectively fuses particles in a powder bed layer by layer. While these processes are capable of producing complex geometries with relatively short build times, their application to structural ceramics is constrained by several well-documented limitations. Ceramic powders have low thermal conductivity and high melting points, which produce steep thermal gradients during laser processing [20]. These gradients induce residual stresses that manifest as warping, cracking, and delamination in the final part [21]. Furthermore, the rapid solidification inherent to laser-based fusion tends to produce microstructures with internal porosity and non-equilibrium phases, both of which are detrimental to mechanical performance [22].

Binder jetting offers an alternative that avoids the high-temperature processing step during fabrication. In BJ, a liquid binding agent is selectively deposited onto a ceramic powder bed to build up green-body geometry, which is subsequently densified through debinding and sintering. A persistent challenge in BJ of ceramics is incomplete coalescence of powder particles during sintering, which leaves residual internal porosity and reduces the achievable theoretical density of the final part [21]. Post-processing treatments such as hot isostatic pressing (HIP) can partially mitigate this limitation, but they add process complexity and cost [23]. For Ce-TZP specifically, the sensitivity of the tetragonal-to-monoclinic transformation to thermal history means that the sintering profile must be carefully controlled to avoid destabilizing the desired phase composition [17], [18].

A general limitation shared across powder-based approaches is that they produce parts with surface roughness and internal microstructural heterogeneity that require extensive post-processing to meet dimensional and mechanical specifications [24]. Powder-based AM techniques share a common dependence on thermally driven consolidation, which introduces several limitations that become particularly pronounced for ceramic systems. These limitations are summarized in Table 2.1.

The shortcomings of powder-based approaches have motivated growing interest in resin-based AM, particularly vat photopolymerization. Unlike slurry-based systems that rely on powder fillers and suffer from light-scattering effects that limit achievable resolution, particle-free photoresins are capable of sub-micrometer resolution and yield green bodies with more homogeneous microstructures [25], [26]. Vat photopolymerization has further been identified as capable of high print speeds, and emerging variants such as volumetric additive manufacturing enable structures with smoother surfaces and improved material isotropy compared to conventional layer-by-layer approaches[27], [28].

Table 2-1: A comparison of powder-based AM techniques

	SLS / SLM	Binder jetting (BJ)
Process principle	Laser or e-beam selectively fuses powder particles in a bed layer by layer (SLM = full melt; SLS = partial)	Liquid binder selectively deposited onto powder bed; green body then sintered or infiltrated
Typical resolution	~50–200 µm (laser spot limited)	~100–400 µm (binder spread limited)
Key limitation for ceramics	High thermal gradients cause residual stress, cracking, and incomplete densification in brittle ceramics	High porosity in green body; sintering shrinkage (15–25%) causes warping and cracking; binder burnout adds complexity
Representative ceramics	Al_2O_3, SiC, ZrO_2, Si_3N_4, hydroxyapatite	Al_2O_3, ZrO_2, SiC, TiO_2, mullite
Densification route	**In-situ (direct)**	**Post-processing**

2.1.2 Resin-Based Additive Manufacturing of Ceramics

Resin-based AM encompasses vat photopolymerization (VP) techniques, principally Stereolithography (SLA) and Digital Light Processing (DLP), as well as direct ink writing (DIW), also referred to as robocasting. These methods process ceramic-loaded resins or pastes and have demonstrated substantially improved surface quality and dimensional accuracy over powder-bed techniques.

The conventional approach in VP-based ceramic AM is to disperse a high-volume fraction of ceramic powder into a photocurable resin to form a ceramic slurry. Upon UV or visible light exposure, the resin polymerizes around the ceramic particles, forming a green body that is subsequently debound and sintered. However, ceramic particles suspended in a resin introduce significant light-scattering effects that degrade cure depth and lateral resolution. For zirconia-based slurries in particular, the high refractive index mismatch between ZrO_2 particles and the surrounding resin ($\Delta n \approx 0.5–0.8$) severely limits achievable resolution to approximately 20 µm under standard SLA/DLP conditions and effectively precludes the use of high-resolution two-photon lithography (TPL) [25]. The light-scattering problem also constrains the maximum

ceramic loading that can be practically processed, limiting the ultimate density and mechanical properties of sintered parts.

Fournier et al. (2023) conducted a comprehensive investigation into the SLA printing of Ce-TZP composites and examined how the processing method affects ductile behavior and transformation features in the sintered ceramic. Their work demonstrated that Ce-TZP printed by stereolithography exhibits a stress-induced tetragonal-to-monoclinic transformation under loading, similar to conventionally processed Ce-TZP, but that the extent and reversibility of this transformation are sensitive to both the ceramic particle size distribution in the slurry and the sintering conditions applied after printing. Notably, parts processed with finer particle distributions and optimized sintering profiles achieved transformation strains and fracture toughness values approaching those of cold isostatically pressed reference specimens, establishing that the functional transformation behavior of Ce-TZP can be preserved through the SLA route when processing parameters are carefully controlled [17].

DIW (robocasting) takes a different approach by extruding a highly concentrated ceramic paste through a nozzle to build up green-body geometry. Unlike VP methods, DIW is not constrained by light-scattering, and the rheological properties of the ink rather than its optical transparency govern processability. For Ce-TZP, early robocasting studies demonstrated the fabrication of 3D-printed 10CeTZP-Al_2O_3 composite architectures and evaluated their mechanical and biological properties [29]. The critical challenge in DIW is ink formulation: the paste must exhibit shear-thinning behavior to flow under extrusion pressure while retaining sufficient yield stress to maintain shape after deposition. Rheological characterization of Ce-ZrO_2 inks has established compositional windows for stable extrusion [30], though achieving high ceramic loading while maintaining printability remains an ongoing challenge.

An alternative resin-based strategy employs inorganic-organic hybrid resins, in which metal complexes or metal salts are dissolved directly into an organic photopolymer matrix rather than dispersed as solid particles. This approach eliminates the light-scattering problem and enables high-resolution photopolymerization, including TPL at sub-micron scales [25]. Gailevičius et al. (2019) demonstrated the TPL printing of glass-ceramic structures at nanoscale resolution using a hybrid organic-inorganic resist, achieving feature sizes below 200 nm. However, inorganic-

organic hybrid approaches are generally limited by a narrow composition window, the need for custom synthesis of non-commercial precursor compounds, and challenges in achieving the high metal-ion concentrations required to produce dense ceramics after pyrolysis and sintering. These constraints have motivated the development of hydrogel-infusion-based routes, which are discussed in detail in Section 2.2.

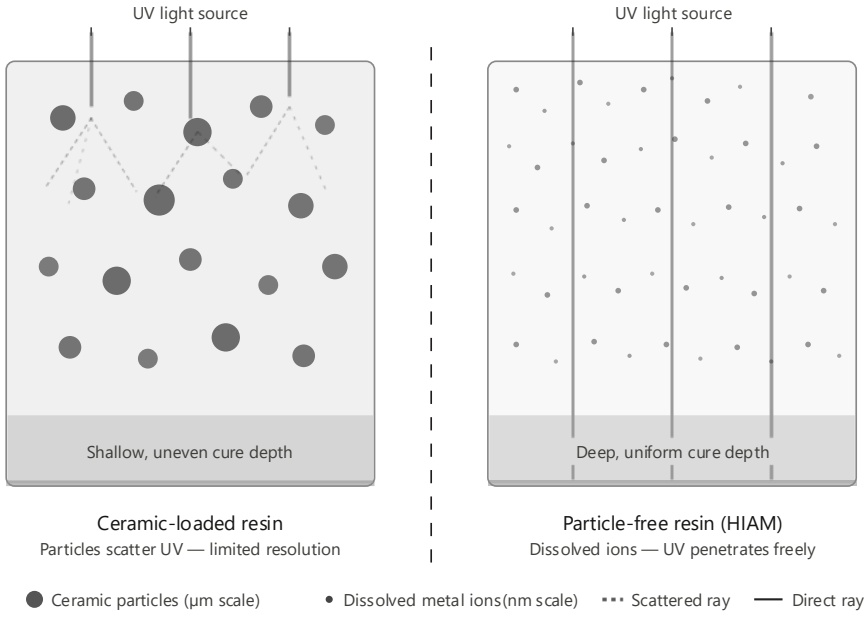

Figure 2-1: Schematic comparison of UV light propagation in a ceramic-loaded resin (left) versus a particle-free hybrid resin (right). Solid particles scatter and attenuate the beam, limiting resolution, while dissolved ions allow free propagation and high-resolution photopolymerization.

2.2 Hydrogel Infusion Additive Manufacturing (HIAM)

2.2.1 Principles and Process Overview

Hydrogel infusion additive manufacturing (HIAM) is a process developed by researcher Julia Greer and coworkers at Caltech that decouples the shape-defining step from the ceramic material introduction step [14]. Rather than processing a ceramic-laden feedstock directly, HIAM first prints a pure polymer hydrogel scaffold using conventional SLA or DLP, then infiltrates that scaffold with metal salt precursor solutions to introduce the ceramic-forming species into the network. The printed hydrogel acts as a swellable, porous template whose three-dimensional

architecture is defined at the printing stage without the optical constraints imposed by ceramic particle loading.

The process proceeds through four principal stages. In the first stage, a hydrogel precursor resin composed typically of poly(ethylene glycol) diacrylate (PEGDA), poly(ethylene glycol) methacrylate (PEGMA), or related monomers is photopolymerized into a three-dimensional scaffold using SLA or DLP.

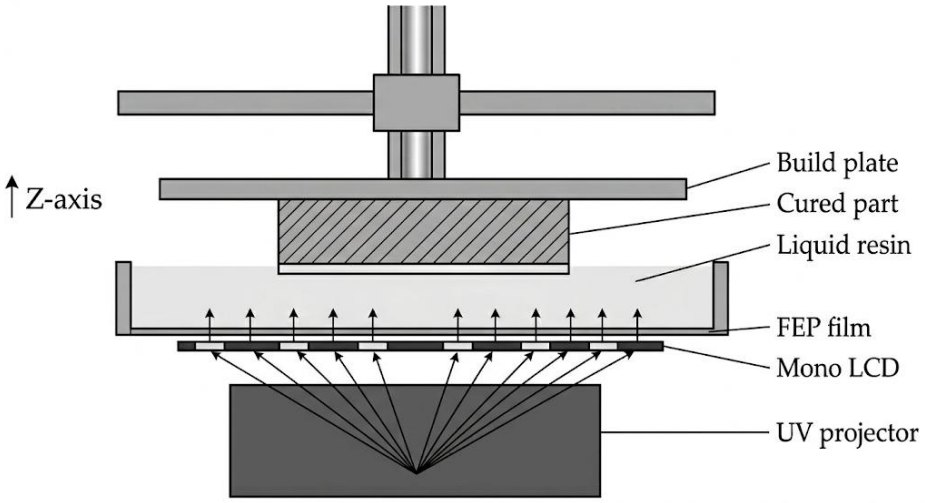

Figure 2-2: Schematic of the cross-section of a bottom-up LCD-DLP printer. UV light is patterned by the LCD and cured through the FEP film layer by layer, with the build plate rising to grow the part.

The network mesh size, swellability, and mechanical stiffness of the resulting hydrogel are governed by the monomer molecular weight, crosslink density, and water content of the resin formulation [31],[32]. In the second stage, the printed hydrogel is immersed in a concentrated aqueous metal salt solution. The hydrogel swells and absorbs the solution, loading metal ions into the polymer network through a combination of osmotic driving force and electrostatic interaction between the ions and the polymer chains [31]. The amount of metal ion uptake is therefore a function of both the equilibrium water content (EWC) of the hydrogel and the maximum achievable concentration of the metal salt precursor solution.

In the third stage, the metal-ion-loaded hydrogel is treated with a precipitating agent, typically ammonium hydroxide or a similar base, which converts the dissolved metal ions into insoluble metal hydroxide or oxide nanoparticles precipitated within the polymer network. This in-situ

precipitation immobilizes the ceramic precursor within the scaffold, preventing redistribution during subsequent thermal processing. In the fourth and final stage, the precipitate-loaded scaffold is thermally processed: calcination at intermediate temperatures removes the organic polymer and converts the metal hydroxide to the corresponding oxide phase, while sintering at higher temperatures densifies the ceramic and establishes the final microstructure and phase composition.

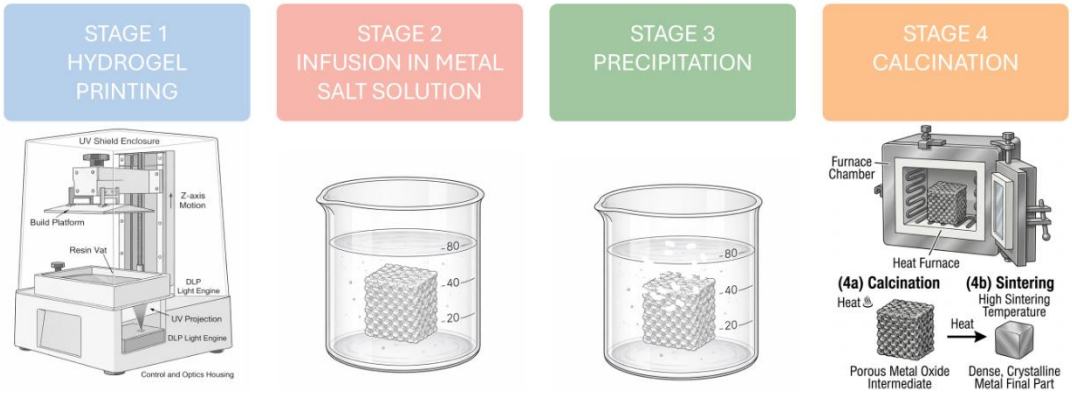

Figure 2-3: Schematic of the four-stage HIAM process: (1) vat photopolymerization of a particle-free hydrogel scaffold, (2) immersion in aqueous metal salt solution to infuse target cations into the polymer network, (3) precipitation to fix the metal ions within the hydrogel, and (4) calcination and sintering to burn off the polymer and densify the ceramic.

The key advantage of HIAM over conventional ceramic AM is that the geometric fidelity of the final part is determined by the hydrogel print, which benefits from the full resolution of standard SLA/DLP without ceramic loading, rather than by a ceramic-laden feedstock. This enables the fabrication of complex three-dimensional lattice architectures, hierarchical structures, and periodic cellular geometries with sub-micron level resolution that would be difficult or impossible to produce through powder-based or slurry-based routes [14]; [33].

2.2.2 HIAM for Metal Oxide Systems

The original demonstration of HIAM by Yee et al. (2019) established the method for a range of functional metal oxides, including NiO, Co_3O_4, Fe_2O_3, and CuO, using nitrate salt precursors and ammonia-based precipitation. The study printed octet-truss and other architected lattice

geometries and demonstrated that the resulting metal oxide parts retained the designed topology after thermal processing, with linear shrinkage in the range of 60–90% relative to the as-printed hydrogel dimensions [14]. This large volumetric reduction arises because the ceramic yield per infusion cycle is limited by the equilibrium water content of the hydrogel and the solubility of the metal salt precursor. When a single infusion-precipitation cycle is used, the total mass of ceramic precursor deposited within the hydrogel is small relative to the mass of the polymer template, and the resulting ceramic after sintering occupies a much smaller volume than the original printed geometry.

Subsequent work extended HIAM to more complex material systems and addressed several of the original method's limitations. Tran et al. (2025) demonstrated HIAM of Cu-Ni binary alloys using co-precipitation of mixed copper and nickel nitrate solutions followed by reduction under a hydrogen atmosphere to produce metallic alloy lattices. Their multiscale characterization revealed that the compositional homogeneity of the resulting alloy at the nanoscale is governed by the relative precipitation kinetics of the two metal hydroxides and the degree of ion mixing within the hydrogel network [34]. This work established that HIAM is extensible to multi-component systems, provided that the co-precipitation chemistry is compatible and that both metal ions are accommodated by the polymer network at sufficient concentrations.

Yaw et al. (2025) investigated precursor design strategies for ceramic HIAM and examined how the choice of metal salt, whether nitrate, chloride, acetate, or organometallic complex, affects precursor solubility, ion-network interaction, precipitation yield, and the phase purity of the resulting oxide after calcination [[35]].

Table 2-2: Summary of prior HIAM demonstrations, organized by generation. First-generation studies (Gen 1) used a single infusion-precipitation cycle and reported linear shrinkage of 60–90%. Second-generation work (Gen 2) by Ji and Yee employed ten sequential cycles, reducing shrinkage to approximately 20% for ceramics and 38% for metals.

Study	Material system	Precursor type	Precipitant used	Infusion cycles	Linear shrinkage
Yee et al. (2019)	Binary metal oxides (ZnO, NiO, Co_3O_4, Fe_2O_3, CuO)	Nitrate salts	Ammonia-based	1	60–90%
Saccone et al. (2022)	Pure metals & alloys (Cu, Ni, Ag, CuNi, CuAg)	Nitrate salts	Thermal calcination / reduction	1	57–73%

Tran et al. (2025)	Cu–Ni binary alloys	Mixed nitrates	-	1	~69%
Ji & Yee (2024/2025) — ceramic	Iron oxide (Fe_2O_3)	Iron chlorides ($FeCl_2$, $FeCl_3$)	Ammonia (NH_3)	10	~20%
Ji & Yee (2024/2025) — metal	Pure iron (Fe)	Iron chlorides ($FeCl_2$, $FeCl_3$)	Ammonia (NH_3)	10	~38%

The studies summarized in Table 2.2 collectively illustrate two distinct phases in the development of HIAM. First-generation work established proof of concept across a range of metal oxide and metallic systems, but at the cost of significant volumetric shrinkage driven by the limited ceramic yield of a single infusion cycle. Second-generation work addressed this directly by repeating the infusion-precipitation sequence, decoupling total metal loading from the hydrogel's initial adsorption capacity and reducing linear shrinkage to approximately 20% in optimized systems.

Precursor selection emerges from this body of work as a critical process variable, governing not only the achievable ion loading but also the phase purity of the calcined product. As Yaw et al. demonstrated, different salt chemistries interact with the polymer network in distinct ways, and some precursor-precipitant combinations produce mixed or undesired phases after thermal treatment. This finding carries direct relevance to the present study: the design of a viable Ce–Zr precursor system must account simultaneously for the solubility constraints of zirconium salts, the differing interaction of Ce^{3+} and Zr^{4+} ions with the PEG network, and the phase requirements of the Ce-TZP system.

Their study demonstrated that precursor selection has a pronounced effect on the achievable metal ion loading and on the crystallographic phase of the calcined ceramic, with some precursor-precipitant combinations producing mixed or undesired phases. This finding is directly relevant to the present work, as the selection of zirconium and cerium precursors for CSZ HIAM must account for both the solubility constraints and the phase requirements of the Ce-TZP system.

The thermal post-processing stage of HIAM for ceramic oxides introduces additional complexity relative to metal systems. Garanin et al. (2025) examined how precursor chemistry and

mineralizer choice affect phase formation in hydrothermally synthesized ZrO_2 nanoparticles, demonstrating that the tetragonal-to-monoclinic phase ratio in the calcined product is sensitive to the identity of the mineralizing agent and to the presence of co-precipitated species [36]. While that study was conducted in the context of hydrothermal synthesis rather than HIAM, its findings are applicable to the HIAM post-processing context because the ceramic nanoparticles formed by in-situ precipitation within the hydrogel network undergo analogous phase transformations during calcination and sintering.

2.2.3 Limitations of HIAM and Recent Advances

The principal limitation of HIAM as originally described is the large linear shrinkage on the order of 60–90% that accompanies thermal processing [14]. This shrinkage arises because the ceramic yield per infusion cycle is limited by the equilibrium water content of the hydrogel and the solubility of the metal salt precursor. When a single infusion-precipitation cycle is used, the total mass of ceramic precursor deposited within the hydrogel is small relative to the volume of the polymer template, and the resulting sintered ceramic occupies a much smaller volume than the original printed geometry.

Yee and coworkers have partially addressed this limitation through the use of multiple sequential infusion-precipitation cycles, in which the scaffold is re-immersed in precursor solution and re-precipitated repeatedly to accumulate additional ceramic mass within the pore network [14]. Each cycle deposits an additional layer of metal hydroxide on the surfaces of previously precipitated particles, gradually increasing the total ceramic loading. While this approach has been shown to reduce linear shrinkage toward approximately 20% in optimized systems, it substantially increases total process time and introduces challenges in maintaining uniform precursor distribution across successive cycles, particularly in complex three-dimensional architectures where diffusion path lengths vary with position.

A further limitation of HIAM, particularly relevant to oxide ceramic systems, is the currently limited body of literature on calcination, sintering, and annealing protocols specifically optimized for HIAM-produced green bodies. Conventional sintering protocols developed for powder-pressed ceramics assume a granular green body with a defined particle size distribution

and packing density, neither of which applies directly to the precipitate-within-polymer architecture produced by HIAM. The distribution of precipitated nanoparticles within the hydrogel network, the residual organic content after debinding, and the local density variations introduced by diffusion-limited precursor uptake all contribute to sintering behavior that may deviate significantly from conventionally processed ceramics of the same composition.

2.3 Potential Challenges of HIAM for Ceria-Stabilized Zirconia

The application of HIAM to ceria-stabilized zirconia introduces several challenges that are specific to this material system and that distinguish it from the metal oxide and metallic alloy systems demonstrated in prior HIAM studies.

The first and most significant challenge is the limited solubility of zirconium salts at high concentrations. Common zirconium precursors including zirconium(IV) oxynitrate ($ZrO(NO_3)_2$), zirconium(IV) chloride ($ZrCl_4$), and zirconium(IV) acetate have substantially lower aqueous solubility compared to the nickel, cobalt, iron, and copper nitrates used in prior HIAM demonstrations [37]; [38]. This low solubility directly limits the metal ion concentration achievable in a single infusion cycle and, consequently, the ceramic mass deposited per cycle. For CSZ HIAM to produce parts with acceptable ceramic yield and manageable linear shrinkage, it is anticipated that a greater number of infusion-precipitation cycles will be required relative to those reported for simpler oxide systems. This multi-cycle requirement increases process duration and demands careful attention to uniformity of precursor distribution in successive cycles.

Table 2-3: Precursor Solubility Comparison

Ion / group	Salt (precursor)	Formula	Solubility (g/100 mL, ~25 °C)	Notes
Zr^{4+}	Zirconium(IV) oxynitrate	$ZrO(NO_3)_2 \cdot 2H_2O$	~25–40	Most common Zr precursor; limited solubility; tendency to hydrolyse
Zr^{4+}	Zirconium(IV) chloride	$ZrCl_4$	Reacts with H_2O	Hydrolyses rapidly; difficult to maintain stable solution
Zr^{4+}	Zirconium(IV) acetate	$Zr(CH_3COO)_4$	~15–20	More stable in solution; chelating character may aid network uptake
Zr^{4+}	Zirconium(IV) acetylacetonate	$Zr(acac)_4$	<5 (poorly soluble)	Organometallic; low water solubility limits use in aqueous HIAM
Ce^{3+}/Ce^{4+}	Cerium(III) nitrate	$Ce(NO_3)_3 \cdot 6H_2O$	>100	Highly soluble; standard Ce precursor in HIAM; stable in solution
Ce^{3+}/Ce^{4+}	Cerium(III) chloride	$CeCl_3 \cdot 7H_2O$	>90	High solubility; used in co-precipitation studies
Ce^{3+}/Ce^{4+}	Cerium(IV) ammonium nitrate	$(NH_4)_2Ce(NO_3)_6$	~100	Ce^{4+} source; strong oxidiser; additional NH_4^+ may affect precipitation
Ni^{2+} *	Nickel(II) nitrate	$Ni(NO_3)_2 \cdot 6H_2O$	>100	Used in Yee et al. (2019) and Saccone et al. (2022)
Co^{2+} *	Cobalt(II) nitrate	$Co(NO_3)_2 \cdot 6H_2O$	>100	Used in Yee et al. (2019)
Fe^{3+} *	Iron(III) nitrate	$Fe(NO_3)_3 \cdot 9H_2O$	>100	Used in Yee et al. (2019) and Ji & Yee (2024/2025)
Cu^{2+} *	Copper(II) nitrate	$Cu(NO_3)_2 \cdot 3H_2O$	>100	Used in Saccone et al. (2022) and Tran et al. (2025)

The second challenge concerns the differential interaction of cerium and zirconium ions with the polymer network. In HIAM, metal ion uptake is governed not only by osmotic swelling but also by the affinity of the ions for the functional groups present on the polymer chains. Cerium (Ce^{3+}/Ce^{4+}) and zirconium (Zr^{4+}) differ substantially in ionic radius, charge, hydration shell structure, and ligand affinity. These differences may produce non-uniform co-precipitation of cerium and zirconium hydroxides within the hydrogel network, leading to compositional heterogeneity in the green body and, ultimately, to phase inhomogeneity in the sintered ceramic. Achieving a homogeneous Ce-Zr distribution at the nanoscale, which is required for consistent tetragonal phase stabilization throughout the part, will therefore require careful optimization of infusion solution composition, precipitation conditions, and possibly the use of chelating agents or co-precipitating additives to promote uniform co-deposition [36]; [35].

The third challenge is the limited prior literature on thermal post-processing of HIAM-produced zirconia structures. As discussed in Section 2.2.3, calcination and sintering protocols for HIAM green bodies differ fundamentally from those for powder-pressed ceramics. For CSZ

specifically, the sintering temperature and atmosphere must be chosen to stabilize the tetragonal phase while achieving sufficient densification. The sensitivity of the Ce-TZP phase composition to sintering conditions, as documented for conventionally processed Ce-TZP [17]; [18], is likely to be amplified in HIAM-produced structures because of the non-uniform nanoparticle distribution and residual porosity present in the green body after debinding. Establishing appropriate calcination and sintering protocols for HIAM-produced CSZ is therefore a non-trivial task that will require systematic experimental investigation.

2.4 Motivation for the Present Study

The challenges outlined in Section 2.3 collectively define the principal barriers to the successful application of HIAM to ceria-stabilized zirconia. Among these, the precursor solubility constraint and its direct effect on ceramic yield and volumetric shrinkage represent the most fundamental obstacle, because no amount of optimization in thermal post-processing can compensate for an insufficient ceramic mass deposited during the infusion stage.

The primary motivation for this thesis study is therefore to establish a viable HIAM process for 3D-printed CSZ lattices by systematically addressing the precursor loading challenge. Specifically, this work aims to identify resin formulations and infusion conditions that maximize the equilibrium water content and metal ion uptake capacity of the printed hydrogel scaffold, in order to pack as high a concentration of cerium and zirconium ions as possible into the network prior to precipitation. By maximizing precursor loading per cycle, the study seeks to reduce the number of cycles required to achieve a target ceramic yield and to limit volumetric shrinkage to a range compatible with dimensional preservation of the designed lattice geometry. The outcomes of this investigation are intended to provide a foundational process window for CSZ HIAM that can be built upon in subsequent studies addressing thermal post-processing and multi-cycle densification strategies.

Chapter 3 Chapter 3: Objectives and Approach

3.1 Research Goal

The goal of this research is to establish a viable process for three-dimensional printing of ceria-stabilized zirconia (CSZ) lattice structures using Hydrogel Infused Additive Manufacturing (HIAM). Zirconia-based ceramics are of significant interest for applications in solid oxide fuel cells, biomedical implants, and MEMS devices, yet current ceramic additive manufacturing methods struggle to deliver both high geometric fidelity and compositional precision simultaneously. By adapting the HIAM framework which can produce 3D structures at a very high resolution, this work seeks to demonstrate that complex zirconia-based ceramic architectures can be fabricated without the resolution penalties of slurry-based resins or the specialized precursor chemistry required by sol-gel two-photon approaches.

3.2 Hypotheses

The following hypotheses guide the experimental design of this study:

- Increasing the PEGDA fraction in the resin raises crosslink density and reduces the effective polymer mesh size, slowing the rate at which metal salt solutions can infuse the hydrogel network. In contrast, increasing the PEGMA fraction reduces crosslink density by introducing pendant methacrylate chains that do not form bridging crosslinks, resulting in a more open network with greater mesh size and higher equilibrium water content that facilitates faster and more extensive ion uptake.
- Increasing the initial water content of the resin produces a more open, swelled network after gelation, resulting in a higher equilibrium water fraction and improved ion uptake capacity.
- Zirconium-containing salt solutions exhibit slower infusion and lower net uptake relative to cerium-only solutions, owing to differences in solution chemistry and the complexation behavior of Zr^{4+} cations with the PEG backbone.
- Multi-stage infusion-precipitation processing improves ceramic yield and reduces net linear shrinkage relative to single-stage infusion, by progressively building up metal loading in situ before thermal conversion.

3.3 Objectives

Three specific objectives are defined to address the research goal:

1. Characterize how modifying the polymer network composition, specifically the PEGMA/PEGDA molar ratio and the initial water content of the resin, affects the equilibrium water content of the swelled hydrogel and its capacity for metal ion loading during HIAM.

2. Investigate the infusion behavior of cerium salt solutions, zirconium salt solutions, and their mixture within the selected hydrogel matrix, and determine whether preferential uptake or differential diffusion kinetics exist between the two cation species.

3. Design and fabricate CSZ lattice structures to demonstrate the feasibility of HIAM for producing geometrically complex, zirconia-based ceramic components.

3.4 Approach

The three objectives are addressed through a corresponding sequence of experimental approaches.

3.4.1 Parametric Study of Resin Composition

A parametric study is conducted using the PEGDA/PEGMA ratio and initial water content as the two primary variables, spanning a 3x3 factorial design across nine resin formulations. The equilibrium water content and effective mesh size of each resulting hydrogel are characterized as functions of these parameters. This systematic mapping of composition-to-structure relationships provides the basis for selecting a resin formulation that maximizes ion uptake capacity while yielding a structurally handleable scaffold.

3.4.2 Infusion Behavior of Ce and Zr Salt Solutions

Using the resin composition identified in the parametric study, infusion experiments are conducted separately for cerium salt solutions, zirconium salt solutions, and their combined mixture. Mass uptake is monitored at successive time intervals throughout each infusion step to quantify infusion kinetics and total ion loading. Comparing these curves across the three solution conditions reveals whether the two cation species diffuse independently or interact, and whether the coordination affinity of Zr^{4+} with the polymer backbone produces measurably different

dynamics from Ce^{3+} or Ce^{4+}. This also identifies whether a multi-stage infusion-precipitation strategy is warranted to improve loading efficiency.

3.4.3 Fabrication of CSZ Lattice Structures

CSZ lattice geometries are designed and printed using the optimized resin formulation and infusion protocol established in the preceding steps. The printed scaffolds are infused with the Ce/Zr salt mixture and thermally processed through calcination. This demonstration closes the loop from process development to functional ceramic fabrication, validating HIAM as a viable route to complex zirconia-based ceramic architectures.

Chapter 4 : Effect of Resin Composition on Hydrogel Network Characteristics

4.1 Motivation

A parametric study was conducted to investigate how the physical characteristics of the hydrogel structure, most critically the polymer mesh size, can be systematically tuned to facilitate more rapid and extensive infusion of zirconium and cerium ions. Understanding the relationship between resin composition and network architecture is essential for optimizing ion uptake capacity and kinetics. In addition to maximizing ion loading, the study was designed to identify formulations that yield structurally coherent, handleable hydrogels, as this is a practical prerequisite for their use in subsequent experimental stages.

4.2 Design of Experiments

The experimental design was developed to identify the optimal resin-to-resin ratio and polymer-to-water ratio that would yield hydrogel structures suitable for ion infusion. Two primary parameters were varied: (1) the molar ratio of poly(ethylene glycol) diacrylate (PEGDA) to poly(ethylene glycol) methacrylate (PEGMA), and (2) the weight fraction of polymer relative to water. A total of nine formulations were prepared across a 3 × 3 factorial design. Exposure times of 10s, 15s and 20s were considered at this stage. Through the experiment, the exposure period that yield the discs wish easy handling and high water content were considered for the next step.

Vials 1–3 were prepared using a 100:0 mol% PEGDA to PEGMA ratio, Vials 4–6 used a 75:25 ratio, and Vials 7–9 used a 50:50 ratio. Within each set of three vials, the water content was varied: the first contained 70 wt% water, the second 50 wt% water, and the third 30 wt% water.

This systematic variation allows for independent assessment of the effects of crosslink density (governed by the PEGDA/PEGMA ratio) and network swelling (governed by water content) on the resultant hydrogel properties.

Table 4-1: Experimental matrix for the parametric hydrogel formation study

Exp	PEGDA/PEGMA (mol%)	Polymer/Water (wt%)
1	100/0	30/70
2	100/0	50/50
3	100/0	70/30
4	75/25	30/70
5	75/25	50/50
6	75/25	70/30
7	50/50	30/70
8	50/50	50/50
9	50/50	70/30

The PEGDA/PEGMA molar ratio and the polymer/water weight fraction were the two main parameters selected for their direct influence on network topology. PEGDA, as a bifunctional crosslinker, forms the primary covalent network; increasing its proportion relative to PEGMA raises crosslink density and reduces mesh size. PEGMA, being monofunctional, introduces dangling chain ends that disrupt network regularity and increase mesh size. Water content, meanwhile, governs the degree of polymer dilution during gelation, thereby affecting the interchain spacing and overall network architecture in the swollen state. Together, these parameters provide a two-dimensional design space for controlling hydrogel porosity and, by extension, ion diffusion behavior.

4.3 Materials and Methods

Hydrogel resins were prepared using poly(ethylene glycol) diacrylate (PEGDA, MW = 700 Da) and poly(ethylene glycol) methacrylate (PEGMA, MW = 480 Da) as the polymer components, with lithium phenyl-2,4,6-trimethylbenzoylphosphinate (LAP) as the photo initiator. Nine formulations were prepared varying two parameters: the PEGDA/PEGMA molar ratio (100/0, 75/25, and 50/50 mol%) and the total polymer-to-water weight fraction (30/70, 50/50, and 70/30 wt%). For each formulation, the polymer components were dissolved in deionized (DI) water, followed by the addition of 1 mL of LAP stock solution (lithium phenyl-2,4,6-

trimethylbenzoylphosphinate, MW = 294.10 g/mol, Sigma-Aldrich, ≥95%), and mixed by sonication until the solution became optically clear.

4.3.2 Curing Procedure

Resin (0.1 mL) was pipetted into PDMS molds of 10mm diameter and 2mm depth. Samples were photocured using a UV lamp (Phrozen Cure and Wash Kit) for curing times of 10, 15, and 20 seconds, which were evaluated across select formulations to assess the effect of curing duration on gel properties.

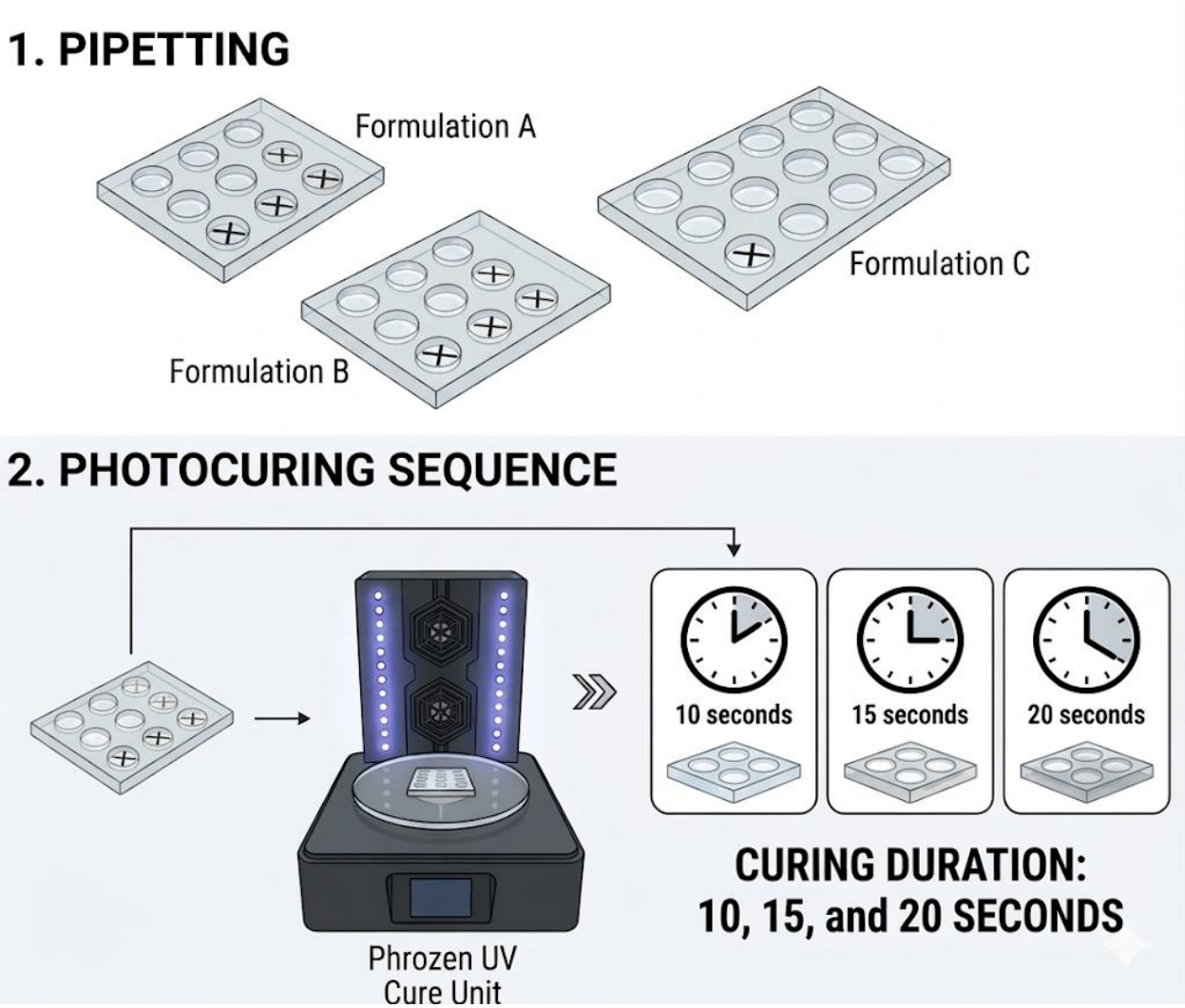

Figure 4-1: Specimen preparation procedure. (1) Resin formulations A, B, and C were pipetted into silicone molds. (2) Each filled mold was cured in a Phrozen UV cure unit at three exposure durations (10, 15, and 20 seconds) to assess the effect of curing time on hydrogel network formation.

4.3.1 Mold Fabrication

PDMS molds were fabricated using a two-part Sylgard 184 silicone elastomer kit mixed at a 10:1 base-to-curing-agent ratio. The mixture was degassed under vacuum to remove air bubbles and cast onto a 3D-printed master mold. The mold was cured in an oven at 65°C for 3 hours and then peeled from the master to yield the final PDMS mold.

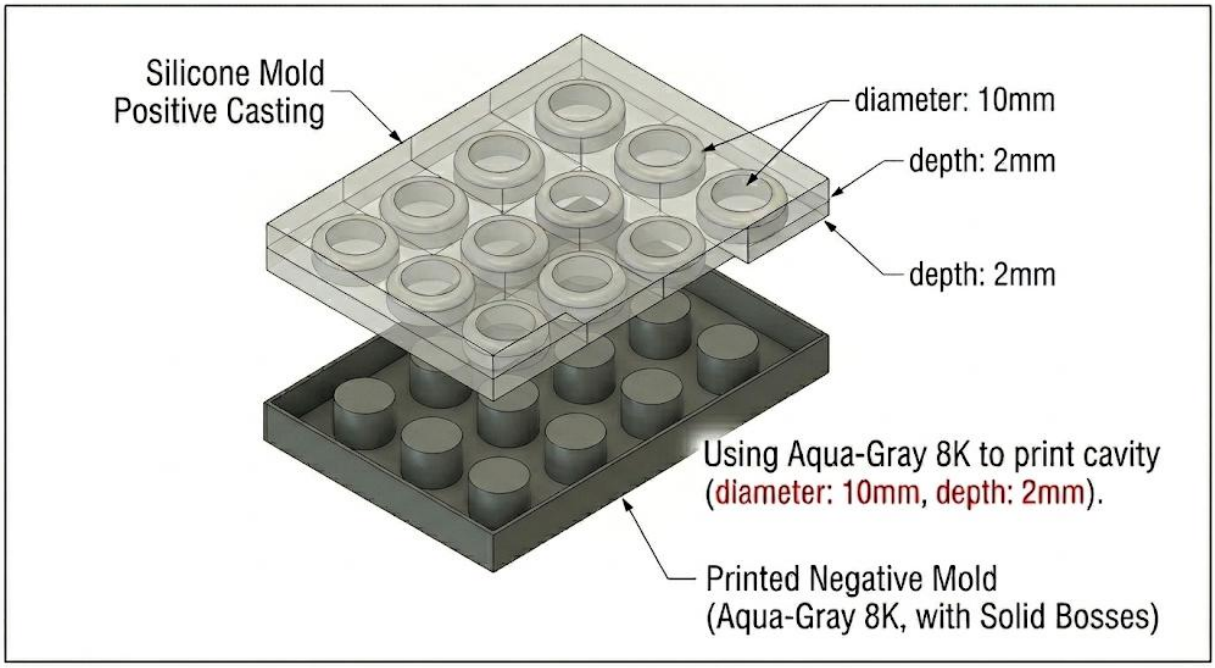

Figure 4-2: Mold fabrication approach for resin specimen casting

4.3.3 Swelling and Water Content Characterization

Following curing, samples were manually assessed for handleability by touch and peeling to qualitatively determine whether the specimens were sufficiently solid. Samples were then weighed immediately after curing to record their initial mass. To assess swelling behavior, cured gels were fully submerged in DI water and allowed to swell overnight (approximately 24 hours) at room temperature, after which the swollen mass was recorded. Samples were subsequently dried in a vacuum oven at 60 °C for 24 hours, and the dried mass was recorded. From these three mass measurements, the following parameters were calculated: swelling ratio (%), drying shrinkage (%), and net mass change (%).

4.4 Results

The equilibrium water content (EWC) of each hydrogel formulation was measured after swelling in deionized water and is reported as the primary characterization metric. EWC was calculated according to:

$$\boldsymbol{EWC}\ (\%) = (\boldsymbol{m}_s - \boldsymbol{m}^d) / \boldsymbol{m}_s \times \mathbf{100}$$

where m_s is the swelled (wet) mass and m^d is the dry mass of the hydrogel. A higher EWC indicates a more open network with greater water-holding capacity, which is expected to correlate with larger effective mesh size and more facile ion diffusion. Results are presented for three UV exposure durations (10 s, 15 s, and 20 s) in Figures 4-3 to 4-5.

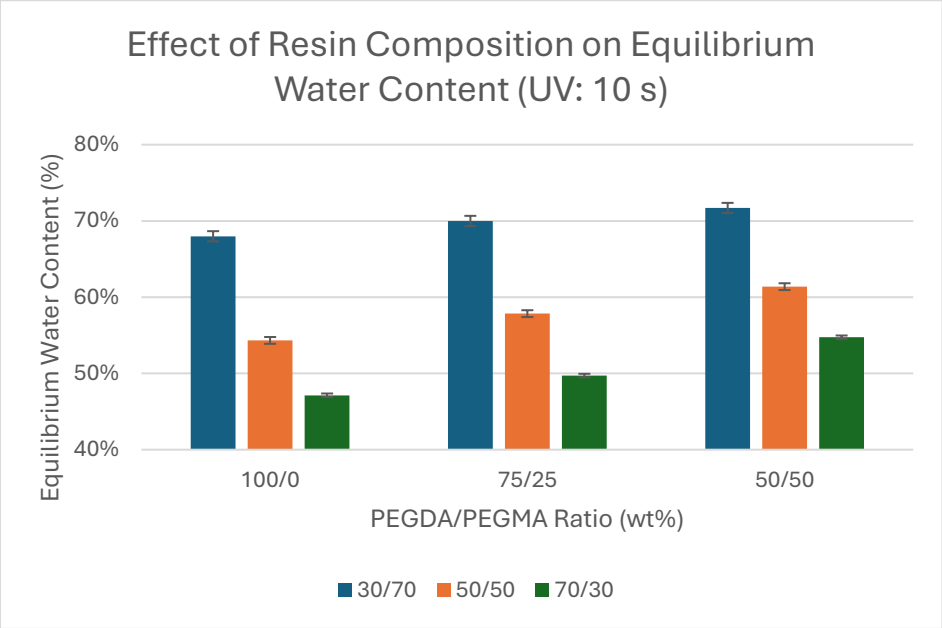

Figure 4-3: Equilibrium Water Content as a Function of PEGDA/PEGMA Ratio and Initial Water Content (10 s UV Exposure)

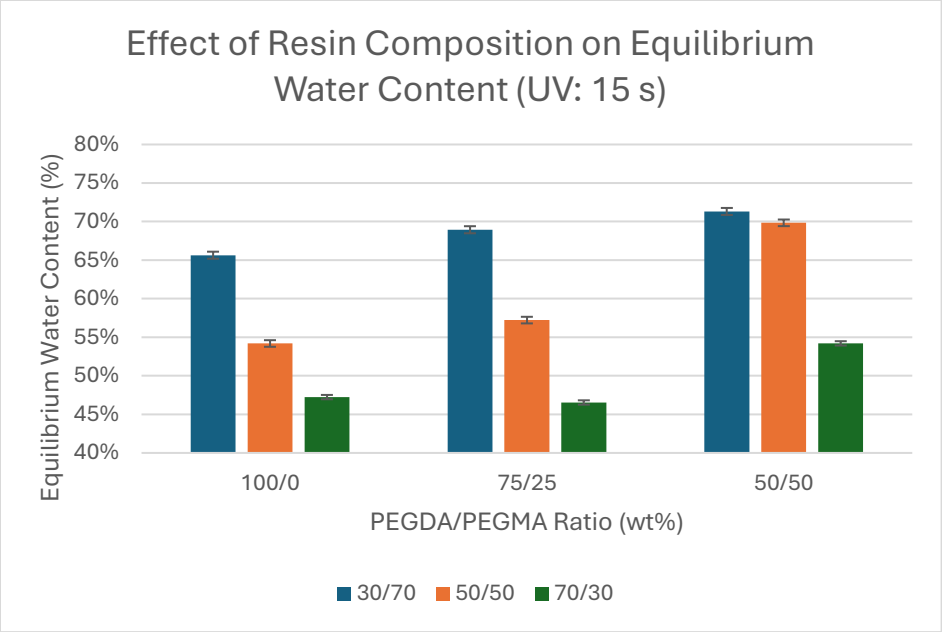

Figure 4-4: Equilibrium Water Content as a Function of PEGDA/PEGMA Ratio and Initial Water Content (15 s UV Exposure)

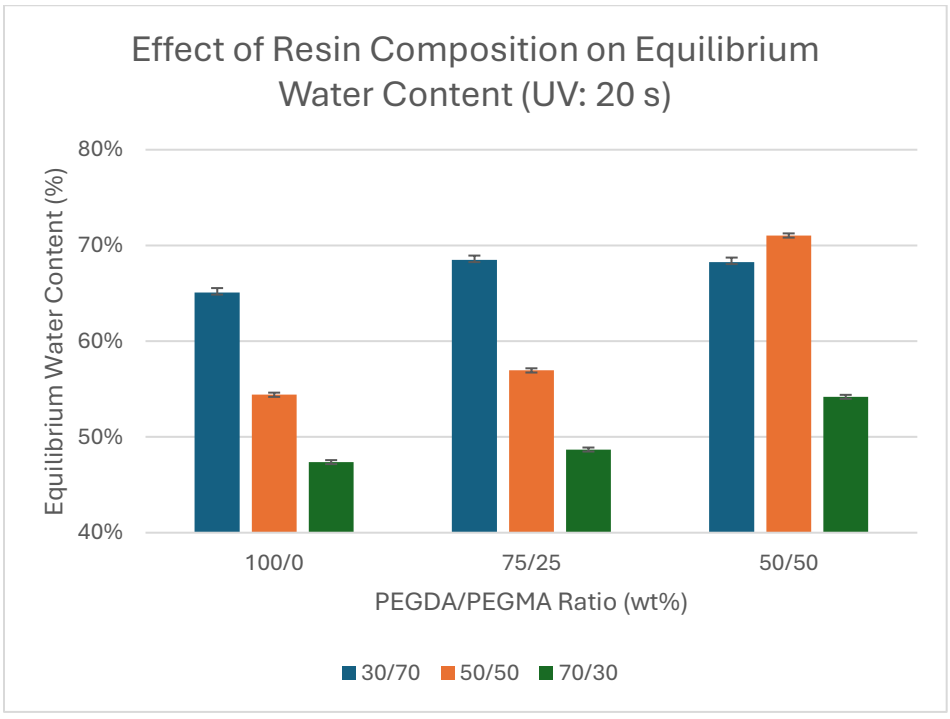

Figure 4-5: Equilibrium Water Content as a Function of PEGDA/PEGMA Ratio and Initial Water Content (20 s UV Exposure)

4.4.1 Effect of PEGDA/PEGMA Ratio

The two monomers used in this study differ fundamentally in their network-forming functionality. PEGDA is a bifunctional crosslinker: it carries a reactive acrylate group at each terminus, allowing it to form covalent bridges between two separate polymer chains simultaneously. PEGMA, by contrast, is monofunctional: one end carries a reactive methacrylate group while the other is terminated by an inert methyl cap, meaning it can incorporate into the network at only one point and contributes a free dangling chain end rather than a crosslink. These structural differences are illustrated in Figure 4-6 [39].

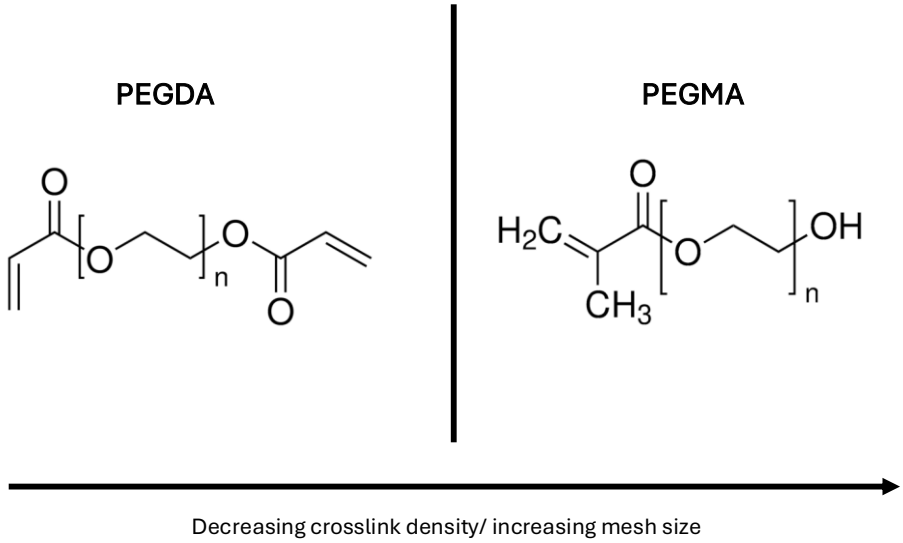

Figure 4-6: Skeletal molecular structures of PEGDA (bifunctional crosslinker) and PEGMA (monofunctional chain extender), with reactive ends and inert terminus labelled

Across all water content conditions and UV exposure durations, EWC increased consistently as the proportion of PEGMA relative to PEGDA increased. At 30/70 polymer-to-water ratio and 10 s UV exposure, for instance, EWC rose from 67.99% for the 100/0 (pure PEGDA) formulation to 71.70% for the 50/50 formulation. This represents an increase of approximately 3.7 percentage points. This trend was preserved at 15 s and 20 s exposures, with the 50/50 formulation consistently recording the highest EWC within each water-content column.

This behaviour is consistent with the known network chemistry of PEGDA/PEGMA systems. As the PEGMA fraction increases, the number of elastically active crosslinks per unit volume

decreases, network regularity is disrupted by the growing population of dangling chain ends, and the effective mesh size ξ increases. The resulting network is more loosely constrained, swells more readily in water, and accommodates a greater volume of solvent within its pores. These structural consequences are illustrated schematically in Figure 4-7 [40]. A larger mesh size is directly relevant to the objectives of this study: a more open network is expected to facilitate faster infusion and higher loading of Zr and Ce ions during the HIAM process.

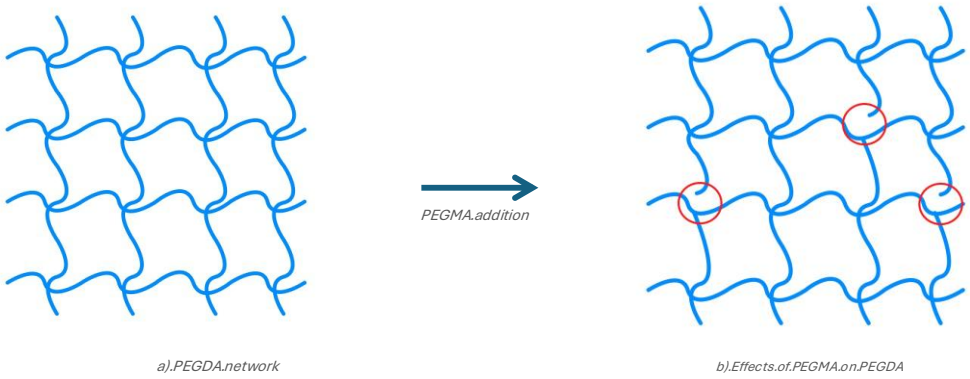

Figure 4-7: Schematic comparison of hydrogel network architecture for high-PEGDA (tight mesh, small ξ) and high-PEGMA (open mesh, large ξ) formulations. 4.4.2 Effect of Starting Water Content

EWC decreased substantially as the polymer-to-water weight fraction increased (i.e., as the initial water content decreased from 70 wt.% to 30 wt.%). For the 50/50 PEGDA/PEGMA formulation at 10 s UV exposure, EWC decreased from 71.70% at 30/70 polymer/water to 54.74% at 70/30 polymer/water which is a reduction of approximately 17 percentage points. This pattern was consistent across all resin ratios and UV exposure durations.

The mechanism underlying this trend relates to the role of water as a porogen during photopolymerization. A higher initial water content dilutes the monomer mixture prior to gelation, promoting a more porous, open network structure as the polymer chains crosslink around a water-rich template. Formulations with high initial water content therefore yield networks with greater free volume and wider interchain spacing in the swollen state. Conversely, formulations with lower initial water content produce more compact networks with higher effective crosslink density per unit volume, resulting in reduced equilibrium swelling.

4.5 Discussion

The results of the parametric study demonstrate that both the PEGDA/PEGMA ratio and the initial water content exert significant, independent influences on the equilibrium water content of the resulting hydrogel and by extension, on the effective mesh size available for ion infusion. Across all conditions, the highest EWC values were consistently observed for the 50/50 PEGDA/PEGMA formulation prepared at 30/70 polymer-to-water ratio, confirming that maximizing PEGMA content and initial water content together produces the most open, hydrophilic network architecture.

Considering UV exposure duration, the 10 s condition for the 50/50 / 30/70 formulation (Vial 7) yielded an EWC of 71.70% which was the highest single value recorded across the entire experimental matrix. Shorter UV exposure results in lower total crosslink conversion, which reduces network density and yields a more permeable structure. While very short exposures risk incomplete gelation and poor mechanical integrity, the Vial 7 formulation at 10 s UV exposure produced a structurally coherent, handleable hydrogel, satisfying the secondary criterion of the study.

On this basis, the formulation corresponding to Vial 7 (50/50 mol% PEGDA/PEGMA resin at 30/70 polymer-to-water weight ratio, photopolymerized under 10 s UV exposure) was selected as the optimal composition for all subsequent infusion experiments. This formulation offers the largest mesh size and highest water uptake capacity within the parameter space investigated, while remaining practically handleable throughout the experimental workflow.

Chapter 5 : Infusion Behavior of Cerium and Zirconium Precursors in HIAM

5.1 Introduction

The preceding chapter established the optimal hydrogel formulation for HIAM of ceria-stabilized zirconia through a 3×3 factorial experimental design evaluating monomer composition, polymer-to-water ratio, and UV exposure time. Analysis of equilibrium water content identified Vial 7 (50/50 PEGDA/PEGMA, 30/70 polymer/water, 10s UV) as the theoretically optimal formulation

based on its network swellability and ion uptake capacity. However, the high water content of Vial 7 produces a hydrogel with insufficient mechanical stiffness during printing to achieve reliable layer resolution on the Phrozen 8K mini printer available. Vial 8 (50/50 PEGDA/PEGMA, 50/50 polymer/water, 10s UV), which uses an equal polymer-to-water ratio, produced consistently better print quality and dimensional stability on this printer while retaining a substantial EWC suitable for salt infusion. Vial 8 was therefore selected as the working formulation for all infusion experiments reported in this chapter.

The central questions motivating this chapter are twofold. First, how rapidly and to what extent do Ce and Zr salt solutions infuse into the hydrogel under ambient and elevated temperature conditions? Second, does the infusion behavior of the two salts differ in ways that are relevant to the co-infusion strategy required for CSZ HIAM? Understanding the kinetics and capacity of salt uptake for each precursor independently is a prerequisite for designing a co-infusion protocol that achieves a homogeneous Ce-Zr distribution within the scaffold. The results presented here also provide an initial assessment of whether multiple sequential infusion-precipitation cycles represent a viable densification strategy for this material system.

5.2 Design of Experiments

Two sets of infusion experiments were conducted to characterize the uptake behavior of Ce and Zr salt solutions. In the first set, ten hydrogel discs fabricated from the Vial 7 formulation were divided into two groups of five: one group was infused in a 2 M $CeCl_3 \cdot 7H_2O$ solution and the other in a 2 M $ZrOCl_2 \cdot 8H_2O$ solution. All infusions in this set were conducted at room temperature. Mass measurements were taken at fixed time intervals (30, 60, 90, and 120 minutes, and overnight) to track the rate and extent of salt uptake relative to the initial swollen mass of each disc.

In the second set of experiments, the infusion procedure was repeated at an elevated temperature of 60°C to assess whether temperature has a significant effect on infusion kinetics and final salt uptake. The same 2 M concentrations were used for both salts to allow direct comparison between the room temperature and elevated temperature conditions.

Infusion behavior was monitored through three complementary approaches: gravimetric tracking via sequential mass measurements, visual observation of structural changes including swelling, surface appearance, and dimensional stability, and thermogravimetric analysis (TGA) to quantify

residual inorganic content after thermal processing. TGA characterization is planned for a subsequent stage of the study; the results presented in this chapter are based on gravimetric and structural observations.

5.3 Materials and Methods

5.3.1 Preparation of Salt Solutions

Cerium(III) chloride heptahydrate ($CeCl_3 \cdot 7H_2O$) and zirconium(IV) oxychloride octahydrate ($ZrOCl_2 \cdot 8H_2O$) were each dissolved in deionized water to prepare 2 M stock solutions. Both salts dissolved readily at room temperature with moderate stirring and produced stable, clear solutions at the target concentration. No precipitation, gelation, or phase separation was observed in either solution during preparation or over the duration of the experiments.

It is worth noting that zirconium salt solutions at higher concentrations are susceptible to hydrolysis and spontaneous precipitation due to the strong tendency of Zr^{4+} to form polynuclear hydroxo complexes in aqueous media [36]. The use of $ZrOCl_2 \cdot 8H_2O$ at 2 M concentration was selected in part because this salt form is more stable in aqueous solution than anhydrous $ZrCl_4$ or zirconyl nitrate under ambient conditions. A citric acid chelation strategy to further stabilize higher-concentration Zr solutions and enable multi-step infusion-precipitation cycles is planned for subsequent experimental stages but was not implemented in the present study.

5.3.2 Infusion Procedure

Hydrogel discs were printed from the Vial 7 formulation and allowed to swell fully in deionized water prior to infusion. Each disc was blotted lightly to remove surface water and weighed to record the initial swollen mass before immersion in the salt solution. Discs were then placed individually in covered containers with sufficient salt solution volume to maintain full submersion throughout the experiment.

For the room temperature experiment, discs were maintained at ambient laboratory conditions (approximately 22°C) and removed for mass measurement at 30, 60, 90, and 120 minutes, and again after overnight immersion (approximately 18 hours). At each time point, each disc was removed from solution, blotted to remove surface solution, weighed on an analytical balance, and returned to its container. Visual observations of disc shape, surface clarity, and dimensional changes were recorded at each measurement interval.

For the elevated temperature experiment, the same procedure was followed with containers placed in a temperature-controlled water bath set to 60°C for the duration of the infusion period.

5.4 Results

5.4.1 Room Temperature Infusion Behavior

Figure 5.1 presents the normalized mass change for both salt systems over the measurement window at room temperature. This initial deswelling phase is consistent with the known behavior of polyelectrolyte-free hydrogels in concentrated ionic solutions [31].

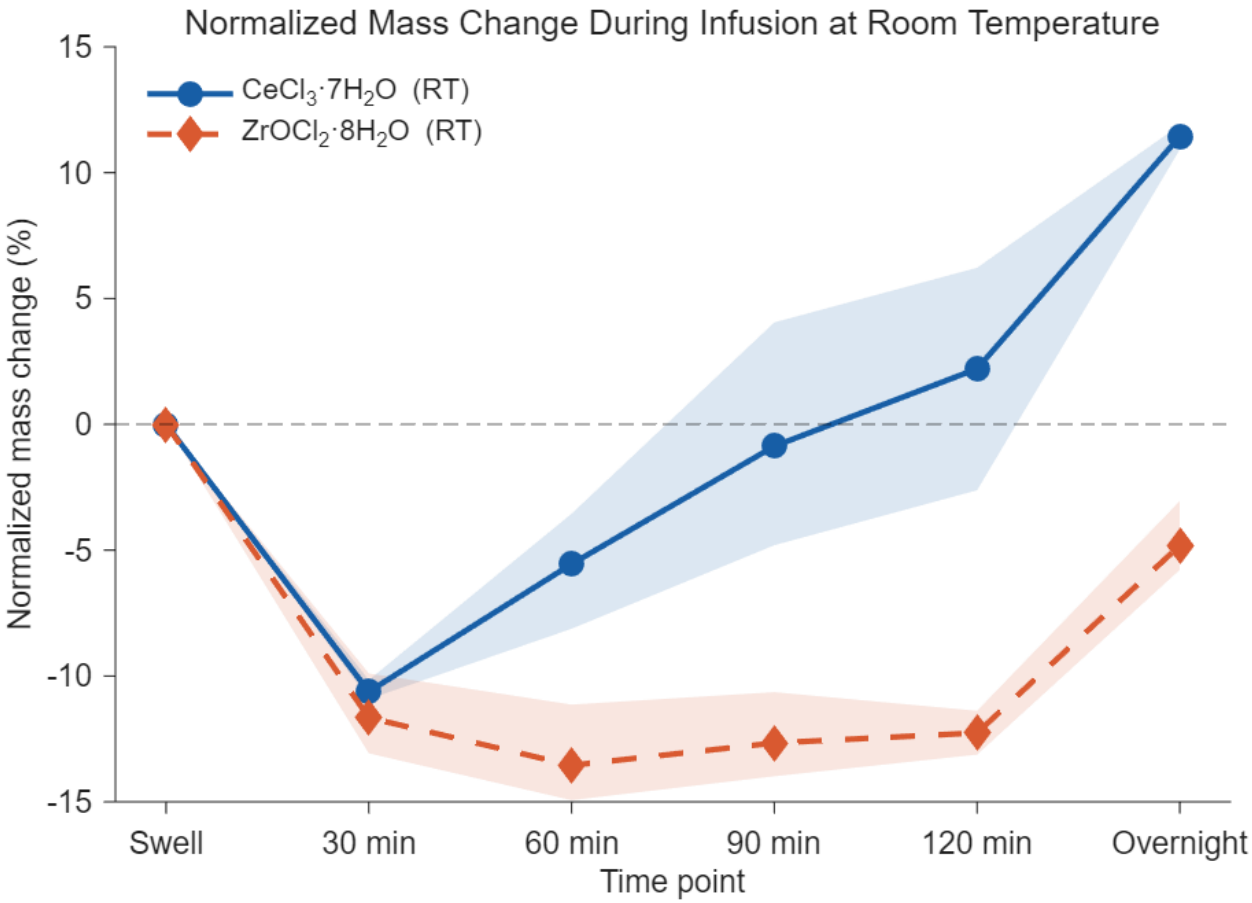

Figure 5-1 Normalized mass change (%) during room temperature infusion for Ce and Zr salt systems.

Both salt systems show an initial mass decrease relative to the swollen baseline at the 30-minute time point. This behavior is attributed to osmotic deswelling: when the hydrogel, which was pre-swollen in deionized water, is transferred to a concentrated 2 M salt solution, the higher osmotic pressure of the external solution draws water out of the network before significant salt ion uptake

occurs as shown in Figure 5-2. This initial deswelling phase is consistent with the known behavior of polyelectrolyte-free hydrogels in concentrated ionic solutions [31].

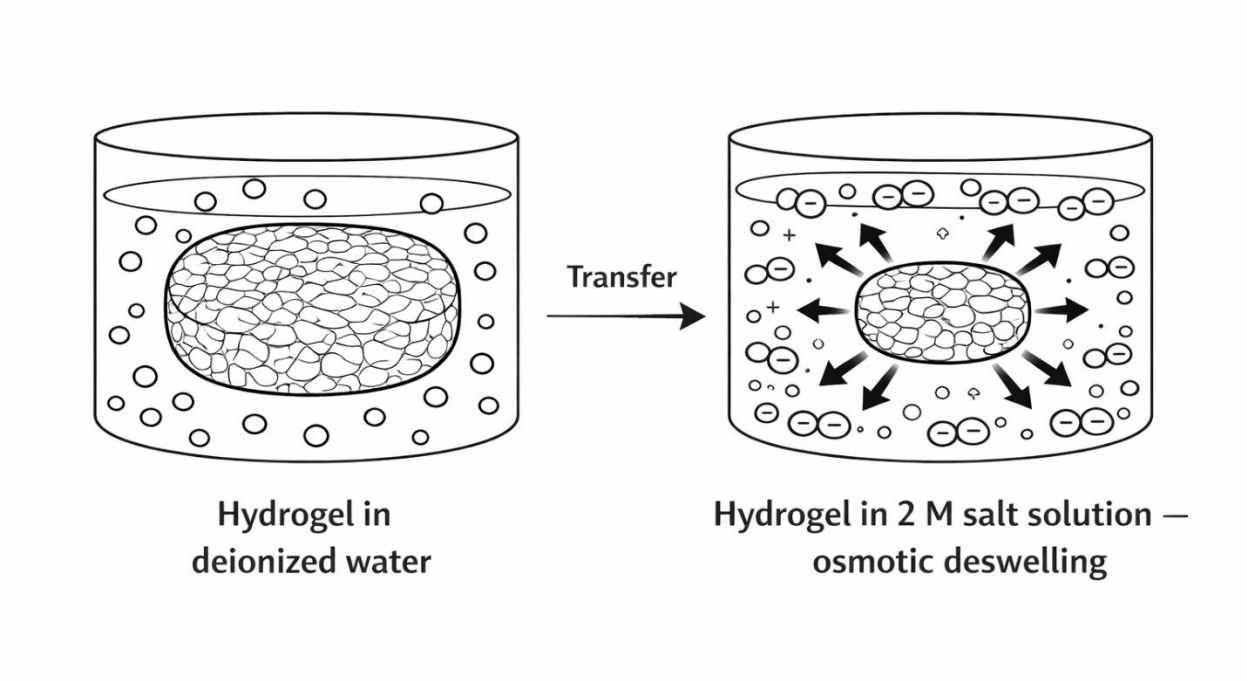

Figure 5-2 Schematic of osmotic deswelling upon transfer of a water-swollen hydrogel to concentrated salt solution

Following the initial deswelling, the two salts exhibit distinct recovery trajectories. The $CeCl_3$-infused discs show a steady and consistent mass recovery from 30 minutes onward, with average mass increasing monotonically through the 120-minute measurement and continuing to increase overnight to an average of 0.1279 g. This value exceeds the initial swollen mass average of 0.1148 g by approximately 11.4%, indicating a net uptake of salt solution into the network over extended infusion time. The trend suggests that Ce^{3+} ions are progressively absorbed into the hydrogel network and that the network reaches a new swelling equilibrium with the salt solution that is higher in total mass than the deionized water baseline.

The $ZrOCl_2$-infused discs display a qualitatively different pattern. After the initial deswelling at 30 minutes, the average mass shows only marginal recovery through the 60 to 120-minute range, with the average remaining near 0.1064 to 0.1079 g across this period. The overnight average of 0.1152 g represents a net gain of approximately 6.7% relative to the initial swollen mass of 0.1230 g, which is notably lower than the Ce system. Furthermore, sample 8 shows no meaningful mass increase between 120 minutes and overnight, and samples 8 and 9 converge to

the same overnight mass of 0.1113 g despite different starting masses, suggesting that the Zr-infused discs may be approaching an equilibrium state at a lower total uptake than the Ce-infused discs.

These differences in infusion behavior between Ce^{3+} and Zr^{4+} are consistent with the difference in ionic charge and hydration shell structure between the two species. Zr^{4+} has a higher charge density and forms larger, more tightly bound hydration shells compared to Ce^{3+}, which may reduce the effective mobility of Zr^{4+} within the hydrogel network and limit its uptake relative to Ce^{3+} at equivalent bulk concentrations.

5.4.2 Elevated Temperature Infusion Behavior

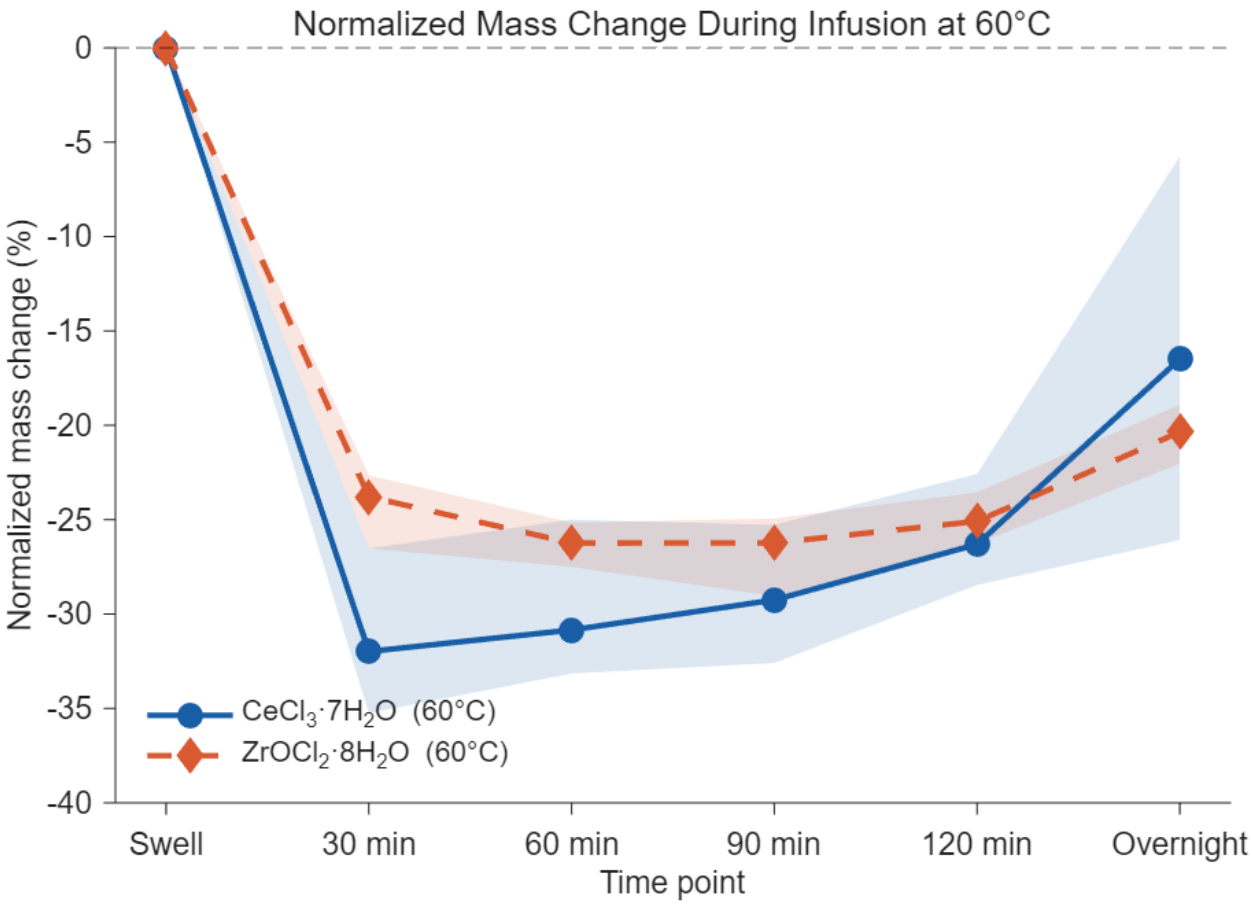

Figure 5-3: Normalized mass change (%) during infusion at 60°C for Ce and Zr salt systems.

Initial deswelling at 60°C is roughly two to three times deeper than at room temperature, with Ce losing ~32% and Zr ~24% of swollen mass at 30 minutes. Neither system recovers to baseline

over the measurement window. Ce ends at a mean of −16.5% overnight with high inter-sample variability (range: −26.1% to −5.8%), while Zr ends at −20.4% with a tighter spread (−22.0% to −18.9%), suggesting a more uniform but persistently compacted network state.

At 60°C, both salt systems exhibit initial osmotic deswelling substantially more severe than at room temperature. The mean normalized mass loss at 30 minutes is −32.0% for Ce and −23.8% for Zr, compared to −10.6% and −11.7% respectively at room temperature. The deeper deswelling at elevated temperature is consistent with the temperature dependence of osmotic activity: higher temperatures increase the chemical potential difference between the concentrated salt solution and the water-swollen network, driving more rapid and extensive water expulsion in the initial minutes of immersion.

In contrast to the room temperature condition, neither salt system recovers meaningfully over the measurement window at 60°C. The Ce system remains near −30% normalized mass through 120 minutes, recovering only to a mean of −16.5% overnight — still far below the swollen baseline and far below the +11.4% achieved at room temperature overnight. The Zr system is similarly constrained, ending at a mean of −20.4% overnight compared to −4.8% at room temperature.

Figure 5.3 presents the normalized mass change trajectories for all four conditions, making clear that elevated temperature suppresses net ion uptake for both precursors rather than enhancing it.

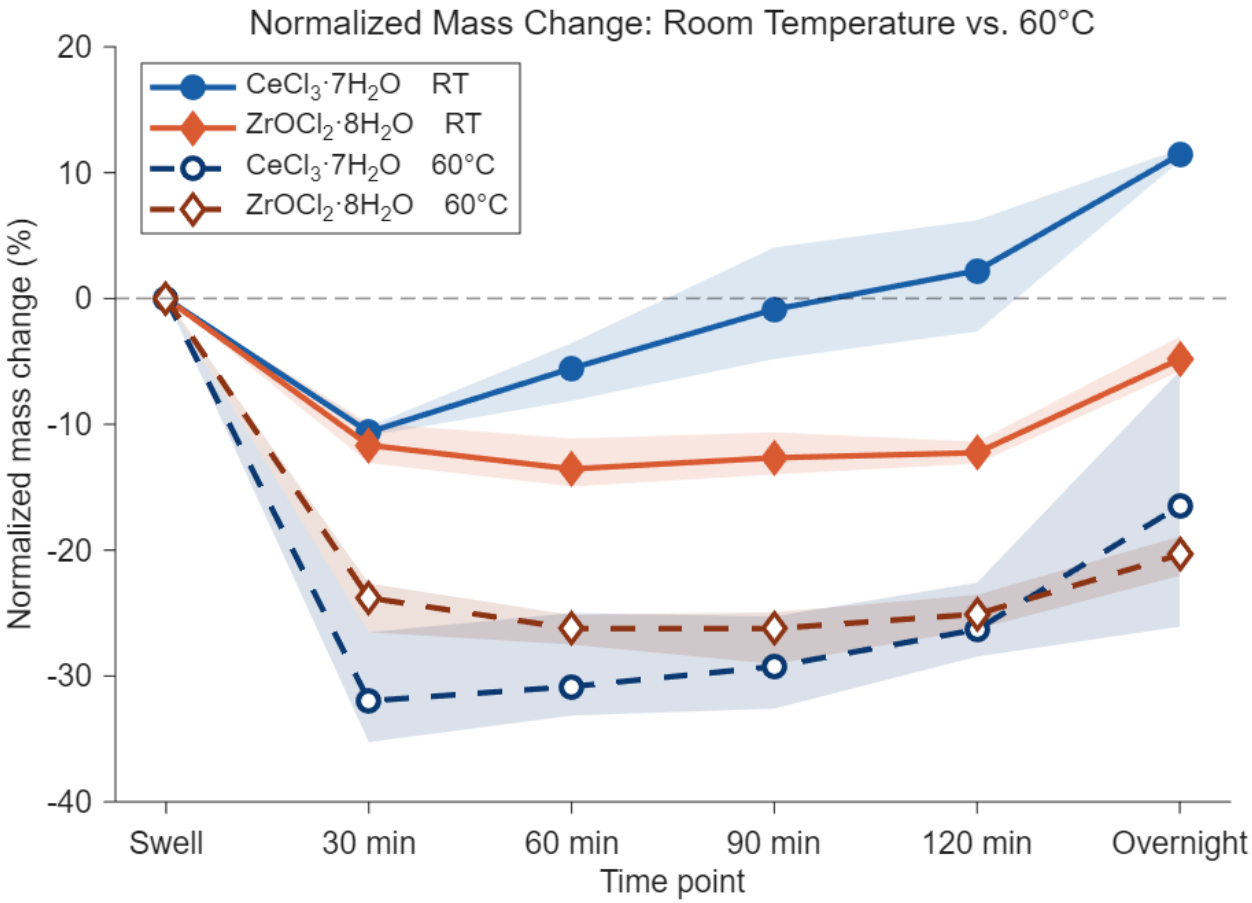

Figure 5-4: Normalized mass change (%) for all four infusion conditions across the measurement window.

Room temperature Ce infusion is the only condition achieving net positive overnight uptake (+11.4%). All 60°C conditions and room temperature Zr remain below the swollen baseline throughout. The comparison demonstrates that elevated temperature suppresses rather than enhances net ion loading for both precursor systems.

The 60°C Ce data also exhibits substantially higher sample-to-sample variability than any other condition tested. The overnight normalized mass range spans from −5.8% to −26.1%, a spread of over 20 percentage points, compared to a range of only 1.0 percentage point for the room temperature Ce group. This dispersion likely reflects differences in the degree to which each disc warped and partially delaminated during heating, altering the effective surface area available for uptake and the internal stress state of the network.

These results reframe the role of temperature in this system. The elevated temperature accelerated infusion kinetics and it actively reduced total ion loading relative to room temperature, likely because the deeper osmotic deswelling at 60°C compacts the network and reduced the available void volume for salt solution re-entry. This led to a reduced geometric fidelity. The implication for HIAM process design is clear that at room temperature infusion is not merely the geometrically safer choice but also the higher performing one for maximizing ceramic precursor loading per infusion cycle.

5.4.3 Implications for HIAM of Ceria-Stabilized Zirconia

The room temperature infusion data establish several points relevant to the design of a multi-cycle HIAM process for CSZ. First, both Ce and Zr precursors can be absorbed into the Vial 7 hydrogel at 2 M concentration without causing structural degradation of the scaffold at room temperature, confirming the basic compatibility of these salt systems with the selected hydrogel formulation.

Second, the lower net uptake of $ZrOCl_2$ relative to $CeCl_3$ at equivalent concentration confirms the concern raised in Chapter 2 that zirconium precursor loading will be the limiting factor in CSZ HIAM. In a co-infusion scenario where both salts are present simultaneously, the differential uptake kinetics and equilibrium capacities of Ce^{3+} and Zr^{4+} are likely to produce a non-uniform Ce:Zr ratio within the network, with Ce preferentially concentrated in regions of higher ion mobility. This has implications for phase homogeneity in the sintered ceramic and underscores the need for careful optimization of co-infusion solution composition and duration.

Third, the overnight data indicate that extended infusion times are required to approach equilibrium uptake, particularly for the Zr system. This suggests that each infusion cycle in a multi-cycle HIAM protocol should include a minimum overnight soak to maximize ion loading before precipitation.

5.5 Discussion

The infusion behavior characterized in this chapter reveals an asymmetry between the Ce and Zr precursor systems that has practical consequences for CSZ HIAM process design. The Ce system

exhibits progressive, monotonically increasing uptake over the measurement window, suggesting that additional infusion time or repeated cycles would continue to increase Ce loading in the network. The Zr system, by contrast, appears to approach an equilibrium plateau at lower net uptake, which limits the Zr ion concentration achievable in a single infusion cycle and reinforces the multi-cycle requirement identified in the literature review.

The precipitation stage of HIAM introduces an additional complexity that has not yet been fully resolved in the present study. Preliminary trials using ammonium hydroxide as the precipitating agent resulted in removal of previously absorbed metal ions from the hydrogel rather than in-situ precipitation within the network. This outcome is likely attributable to the strong complexing affinity of ammonia for Ce^{3+} and Zr^{4+} ions, which can form soluble ammine or hydroxo complexes under excess ammonium conditions and effectively re-dissolve the precipitate rather than fixing it within the network. Identifying a precipitation protocol that produces stable, network-anchored metal hydroxide nanoparticles without displacing previously loaded ions is a critical next step for this work. Alternative precipitation strategies, including the use of dilute base addition, controlled pH titration, or a citric acid chelation approach to pre-stabilize Zr ions prior to precipitation, will be evaluated in subsequent experiments.

The warping observed under elevated temperature infusion conditions also merits further investigation. While 60°C accelerates diffusion and may be useful for shorter infusion cycles in a multi-cycle protocol, the geometric distortion it produces must be mitigated before it can be incorporated into a HIAM process for architected lattices. Possible strategies include using thicker scaffold geometries that are more resistant to differential thermal stress, constraining discs mechanically during infusion, or using a lower intermediate temperature such as 40°C to partially capture the kinetic benefit while reducing thermal stress.

Taken together, the results of this chapter confirm that room temperature overnight infusion at 2 M concentration provides the most reliable and geometry-preserving infusion condition for both Ce and Zr precursors in the Vial 7 hydrogel system. The differential uptake behavior of the two ions establishes a clear motivation for subsequent work on co-infusion optimization and precipitation protocol development, both of which are necessary to advance toward a complete multi-cycle HIAM process for CSZ.

Chapter 6 : Demonstration of HIAM 3D printing of Zirconia-based Ceramic Lattices

6.1 Introduction

The preceding chapters established two critical foundations for the hydrogel-infused additive manufacturing (HIAM) of ceria-stabilized zirconia (CSZ): a resin formulation with sufficient equilibrium water content and printability (Chapter 4), and a characterization of cerium(III) salt infusion behavior into the selected hydrogel network (Chapter 5). The present chapter applies this knowledge to the primary objective of this thesis: the demonstration of HIAM fabrication of zirconia-based ceramic lattice structures.

Lattice architectures offer several advantages over dense monolithic ceramics that make them attractive for structural and functional applications. By distributing material along load-bearing struts or sheets rather than filling a volume uniformly, lattice structures achieve high specific stiffness and strength at reduced density [41]. In addition to mechanical benefits, the open pore network of a lattice provides high surface area and controlled permeability, properties relevant to filtration, catalysis, and thermal management applications in which zirconia-based ceramics are already established materials [42].

Among the many possible lattice topologies, the gyroid minimal surface was selected for this study for several reasons. The gyroid is a triply periodic minimal surface (TPMS), a class of geometries defined by surfaces of zero mean curvature that repeat periodically in three orthogonal directions [43]. TPMS-based architectures have attracted considerable interest in the additive manufacturing literature because their smooth, continuously curved geometry avoids the stress concentrations associated with sharp nodes and strut intersections found in truss-type lattices, resulting in more uniform stress distributions under load [44].The gyroid topology in particular exhibits mechanical near-isotropy, meaning its stiffness and strength are relatively insensitive to the direction of applied load, which is a desirable property for structural applications where loading direction may be variable or unknown [45].

From a manufacturing perspective, the gyroid also presents one of the most demanding geometric tests for a vat photopolymerization process. Its internal channels are fully enclosed

and interconnected, precluding the removal of uncured resin by simple drainage and requiring that the process achieve sufficient cure depth and resolution to render thin walls accurately across the entire part height. Successfully printing a gyroid lattice in a hydrogel resin therefore constitutes a meaningful benchmark for the resolution and reliability of the HIAM process as applied in this study.

This chapter describes the design of the gyroid lattice, the printing and infusion procedures employed, the challenges encountered during fabrication, and the mass evolution of the two successfully fabricated structures through the full HIAM process sequence: infusion, two sequential ammonium vapor precipitation cycles, washing, and vacuum drying.

6.2. Materials and Methods

6.2.1 Resin Formulation

The resin formulation used throughout this chapter was the working formulation identified in Chapter 4: a 50/50 mass ratio of poly(ethylene glycol) diacrylate (PEGDA, Mn 700 g/mol, Sigma-Aldrich) to poly(ethylene glycol) methacrylate (PEGMA, Mn 360 g/mol, Sigma-Aldrich), diluted to a 50/50 polymer-to-water mass fraction, with lithium phenyl-2,4,6-trimethylbenzoylphosphinate (LAP, Mn 288.24 g/mol, Sigma-Aldrich) as the photoinitiator. This formulation, designated Vial 8 in the parametric study of Chapter 4, was selected on the basis of its printability on the available hardware. The formulation with the highest measured equilibrium water content (Vial 7, 30/70 polymer/water) was found to be incompatible with the printing constraints of the Phrozen Sonic Mini 8K due to its lower polymer content and correspondingly reduced mechanical green strength; this tradeoff is discussed further in Chapter 7.

6.2.2 Lattice Design

A gyroid minimal surface lattice was designed for this study. The gyroid is a triply periodic minimal surface defined by the approximate level-set equation:

$$\sin(x)\cos(y) + \sin(y)\cos(z) + \sin(z)\cos(x) = t$$

where t is a value that controls wall thickness and volume fraction. The overall part dimensions were 10 mm x 10 mm x 10 mm with a unit cell size of 2.5 mm, yielding a 4 x 4 x 4 array of unit cells within the part. The geometry was designed to test the resolution limits of the Phrozen Sonic Mini 8K and to produce a structure with sufficient open porosity to allow the infusion solution to penetrate the interior of the lattice without obstruction.

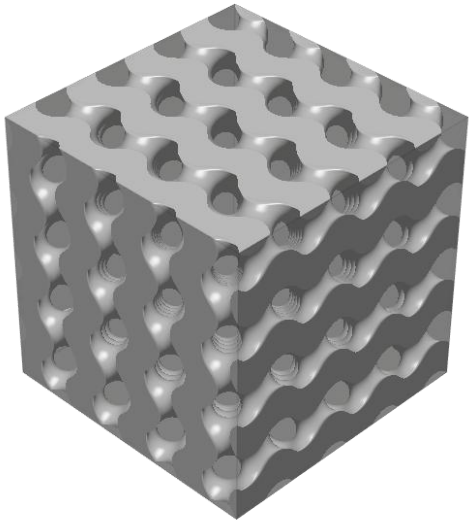

Figure 6-1: — CAD rendering of the 10 x 10 x 10 mm gyroid lattice (2.5 mm unit cell)

6.2.3 Printing Parameters and Procedure

Lattice structures were printed on a Phrozen Sonic Mini 8K DLP photopolymerization printer which uses a bottom-up architecture in which each layer is cured against an FEP-lined resin vat and the build plate retracts upward after each exposure. The printer was sliced using Chitubox software. Printing parameters are summarized in Table 6.1.

Parameter	**Value**
Layer height	0.025 mm
Exposure time (body layers)	19.000 s
Bottom layer count	6
Bottom exposure time	75.000 s

Parameter	Value
Transition layer count	12
Transition type	Linear
Transition layer interval time difference	4.308 s
Lifting distance (bottom / body)	6.0 mm
Lift speed (bottom / body)	40.0 mm/min
Retract speed	100.0 mm/min

Table 6.1. Printing parameters used for gyroid lattice fabrication on the Phrozen Sonic Mini 8K.

Prior to printing, the resin was prepared fresh and loaded into the vat. The build plate was leveled and surface-treated to promote adhesion. Approximately 40 print attempts were made before two structurally intact gyroid lattices were successfully obtained. Four distinct failure modes were identified and documented across these attempts, each arising from a fundamental mismatch between the curing kinetics of the water-rich hydrogel resin and the demands of the bottom-up DLP process (Figure 6.2).

Delamination, in which the partially cured structure detached from the build plate and remained in the resin vat, was the most consequential failure mode. It was driven by a combination of weak initial adhesion, high oxygen inhibition at the resin-FEP interface [46], and low crosslink density resulting from the high water content of the Vial 8 formulation [47]. Feature loss and resolution failure occurred when fine gyroid struts did not resolve or fractured during or after removal from the vat, a consequence of both insufficient cure depth [48] and the reduced mechanical green strength of the hydrated network compared to conventional photopolymer resins [49]. Gel-like deformation produced geometrically inaccurate parts in which premature swelling of the low-crosslink-density network occurred during printing before full curing was achieved [14]. Incomplete builds, in which only a fraction of the structure bonded to the build plate in the early layers, reflected inadequate exposure energy in the bottom layers for a resin of this water content and reactivity [50].

Peel-induced mechanical failure, in which structures tore or distorted during layer separation from the FEP film, was a contributing mechanism across several of the failure modes described above,

directly attributable to the tensile peel force inherent to the bottom-up architecture exceeding the cohesive strength of the partially cured hydrogel [50].

Mitigation strategies were applied iteratively over the course of the print attempts. Bottom layer exposure time was increased substantially (75 s, versus 19 s for body layers) to improve initial adhesion. A 12-layer linear transition from bottom to body exposure time was introduced to reduce the abrupt stiffness change at the interface between the heavily cured base and the standard body layers, which had been observed to act as a fracture initiation site [51]. Lift speed was reduced to 40 mm/min to lower the instantaneous peel force during layer separation [39]. These adjustments, summarized in Table 6.1, were sufficient to produce two viable structures but did not eliminate the underlying incompatibility between bottom-up peel force and the mechanical properties of the hydrogel green part.

The planned approach for future work involves a top-down DLP configuration, in which the light source projects downward through a transparent build window and the part grows downward into the resin vat. This geometry eliminates the peel force entirely, as the part does not need to separate from the projection surface between layers. The anticipated availability of this equipment during the study period was delayed, and the bottom-up Phrozen was used as an alternative. This distinction and its implications for process yield are discussed in Chapter 7.

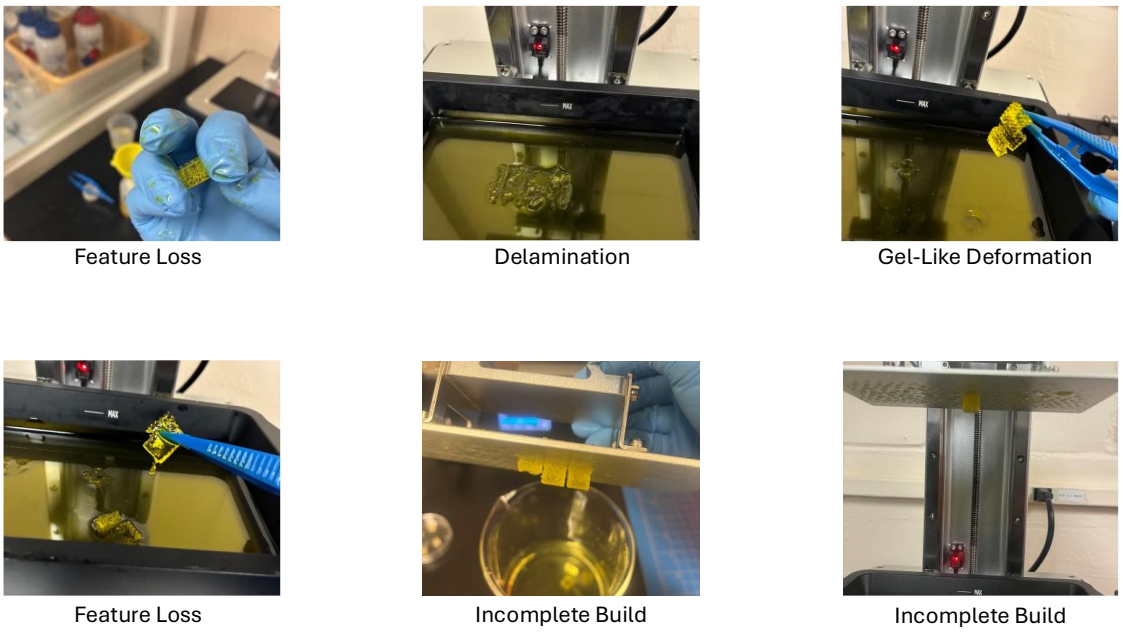

Figure 6-2: Observed failure modes during DLP printing of PEGDA/PEGMA hydrogel gyroid lattices on the Phrozen Sonic Mini 8K

Four distinct failure modes were documented across approximately 40 print attempts, with feature loss (top left, bottom left) and incomplete build (bottom center, bottom right) each illustrated by two representative examples. Feature loss occurred when fine gyroid struts failed to resolve or fractured during handling, attributable to insufficient cure depth and the low mechanical green strength of the water-rich network. Delamination (top center) resulted in complete float-off of the structure from the build plate, driven by weak initial adhesion and high oxygen inhibition at the resin-FEP interface. Gel-like deformation (top right) produced bloated, geometrically inaccurate parts as premature swelling of the low-crosslink-density network occurred before full curing was achieved. Incomplete builds arose when only a fraction of the structure adhered to the build plate in the bottom layers, reflecting a mismatch between the low reactivity of the dilute resin and the exposure energy delivered at early layers.

6.2.4 Infusion

Following printing, each successful lattice was removed from the build plate, rinsed briefly with deionized water to remove uncured resin, and immersed in a 2 M aqueous solution of cerium(III) chloride heptahydrate ($CeCl_3 \cdot 7H_2O$, Sigma-Aldrich) at room temperature. The infusion procedure followed the protocol established in Chapter 5. Samples were weighed at 30 minutes,

60 minutes, overnight (~12 hours), and 48 hours after the onset of infusion to track mass uptake. Prior to each weighing, samples were removed from the solution, blotted dry with a lint-free tissue, and briefly air-blown to remove surface solution, then immediately weighed on a Sartorius analytical balance (0.0001 g resolution). After the infusion period was complete, the lattice was returned to the solution for the interval preceding the next measurement. The 48-hour measurement was used as the endpoint of the infusion stage, consistent with the plateau behavior observed for cerium salt infusion in Chapter 5.

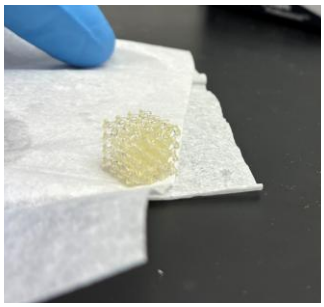

a) lattice pre-infusion

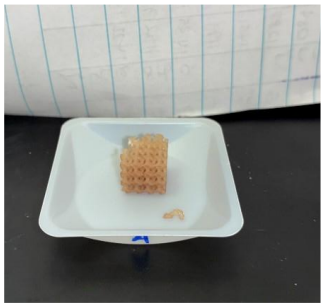

b) lattice post-infusion

Figure 6-3: Photograph of gyroid lattice before infusion (clear/white) and after infusion (yellow-orange coloration from Ce3+ ions)

6.2.5 Precipitation

Two sequential ammonium vapor precipitation cycles were performed following the method described by Yee et al [14]. In each cycle, the infused lattice was first weighed (designated pre-precipitation mass), then placed in a sealed container in the presence of concentrated ammonium hydroxide and exposed to ammonium vapor for 30 minutes. The ammonia vapor diffuses into the hydrogel network and reacts with the dissolved Ce^{3+} ions to form cerium hydroxide precipitates in situ. Following vapor exposure, the lattice was removed, washed twice with deionized water, and sonicated to remove loosely bound surface precipitate. The sample was then surface-dried and weighed (post-precipitation mass) before being re-infused in fresh 2 M $CeCl_3 \cdot 7H_2O$ solution in preparation for the second precipitation cycle. The same vapor exposure, wash, sonication, and weighing procedure was repeated for the second cycle.

After the second precipitation cycle, samples were weighed, then placed in a vacuum oven (Yamato ADP-300C) and dried overnight at 60°C under vacuum. Final mass was recorded after vacuum drying.

lattice after Precipitation Cycle 1

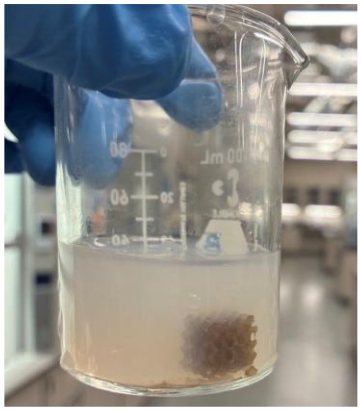

lattice after Precipitation Cycle 2

Figure 6-4: Gyroid lattice after the first (left) and second (right) ammonium vapor precipitation cycles

6.3 Results

6.3.1 Printed Lattice Morphology

Two gyroid lattice specimens were successfully fabricated from the Vial 8 hydrogel resin using the parameters described in Section 6.2.3. Both structures retained the overall 10 x 10 x 10 mm geometry and displayed the characteristic saddle-surface channel network of the gyroid topology in visual inspection. The structures exhibited the translucent, hydrated appearance typical of PEGDA/PEGMA hydrogel networks. Build plate adhesion and lattice integrity were confirmed by visual examination immediately after printing and after the initial water rinse.

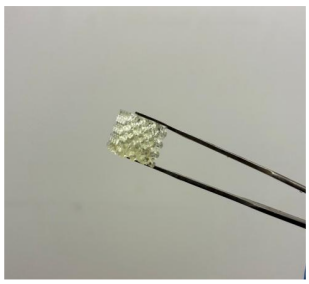

a) Successfully printed gyroid

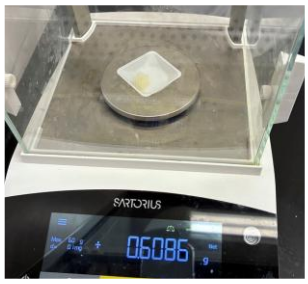

b) Gyroid A – infused

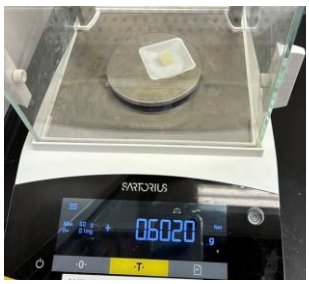

c) Gyroid B – infused

Figure 6-5: Photographs of the successful gyroid hydrogel structures

6.3.2 Mass Evolution Through the HIAM Process

The mass of both specimens was recorded at each stage of the HIAM process sequence: dry (as-printed, post-rinse), at four infusion time points, before and after each precipitation cycle, and

before and after vacuum drying. All masses were recorded after surface drying with a lint-free tissue and brief air blow to remove surface solution. Results are summarized in Tables 6.2 and 6.3.

Sample	Dry (g)	30 min (g)	60 min (g)	Overnight (g)	48 hr (g)
A-1	0.4749	0.5442	0.5791	0.6086	0.6157
A-2	0.4684	0.5346	0.5505	0.6020	0.5821

Table 6.2. Mass (g) of gyroid lattice specimens at each infusion time point. Masses recorded after surface drying.

Both specimens showed a monotonic increase in mass over the infusion period, with the rate of uptake decreasing substantially after the 60-minute measurement. The mass gain from overnight to 48 hours was marginal for both specimens (A-1: 0.6086 to 0.6157 g; A-2: 0.6020 to 0.5821 g, the latter showing a slight decrease likely attributable to measurement variability at near-saturation conditions), consistent with the plateau behavior observed for $CeCl_3$ infusion into disc specimens in Chapter 5. This suggests that the infusion kinetics of the gyroid lattice are comparable to those of the flat disc geometry despite the more complex channel architecture, and that overnight infusion is sufficient to approach equilibrium loading in this system.

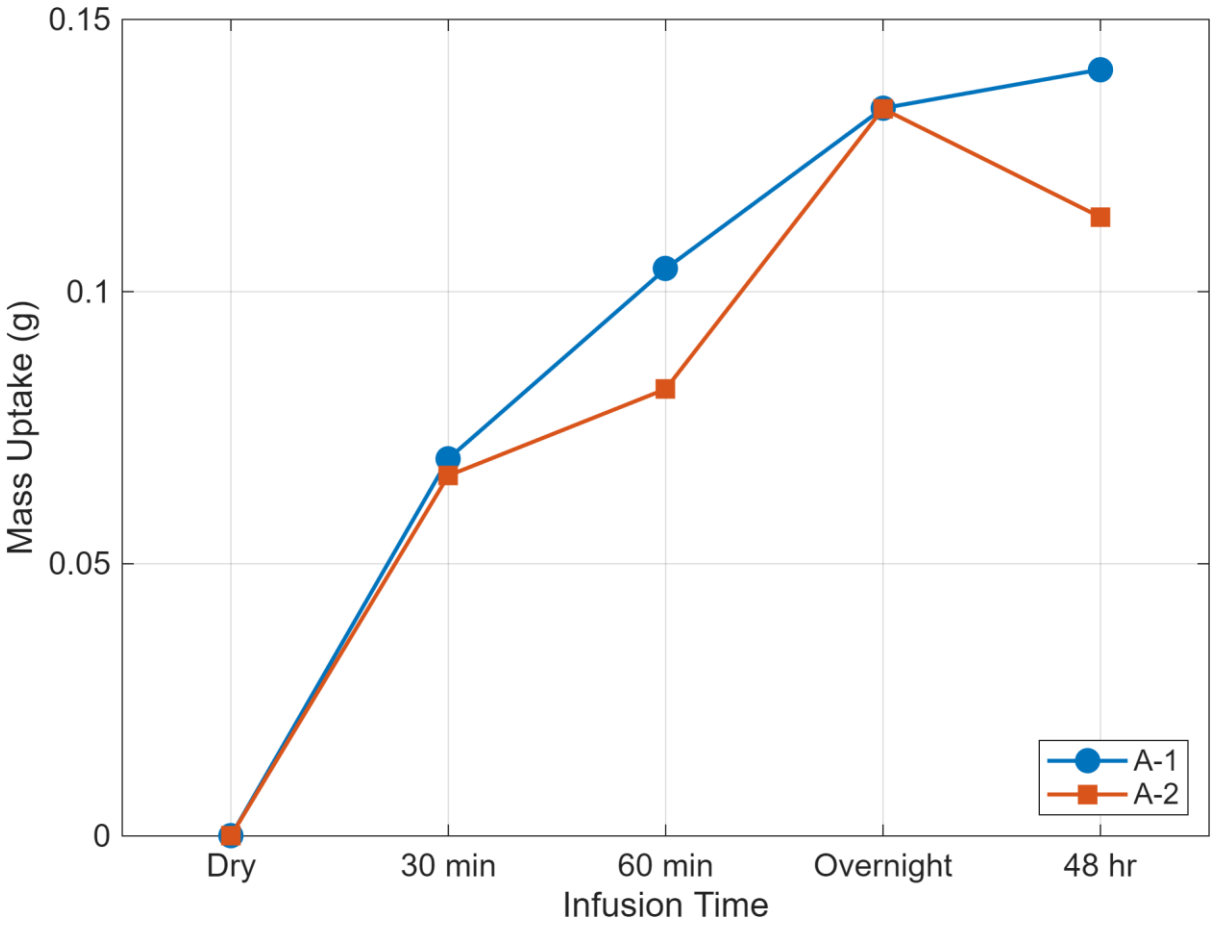

Figure 6-6: Mass uptake of gyroid lattice specimens during infusion in 2 M $CeCl_3 \cdot 7H_2O$ at room temperature

The rate of mass gain decreases substantially after 60 minutes, approaching saturation by overnight, consistent with the plateau behavior observed for cerium salt infusion in Chapter 5 disc specimens.

Table 6-1: Mass (g) of gyroid lattice specimens through the precipitation and post-processing stages

Sample	Pre-Precip 1 (g)	Post-Precip 1 (g)	Pre-Precip 2 (g)	Post-Precip 2 (g)	Pre-Vacuum (g)	Post-Vacuum (g)
A-1	0.6971	0.5775	0.7000	0.7847	0.6413	0.4269
A-2	0.6869	0.5369	0.7000	0.7874	0.7431	0.3720

After Precipitation Cycle 1, both specimens lost mass relative to their pre-precipitation values (A-1: 0.6971 to 0.5775 g; A-2: 0.6869 to 0.5369 g), consistent with partial removal of dissolved Ce^{3+} from the network by conversion to insoluble cerium hydroxide and subsequent washing. The pre-

Precipitation Cycle 2 masses (both recorded as 0.7000 g) reflect re-infusion of the washed specimens in fresh $CeCl_3$ solution, restoring or slightly exceeding the pre-Precipitation Cycle 1 loading. Following the second precipitation cycle, post-precipitation masses increased substantially over Cycle 1 values (A-1: 0.7847 g; A-2: 0.7874 g), indicating that the second cycle deposited additional cerium hydroxide within the network. This result demonstrates the cumulative loading effect of sequential infusion-precipitation cycles [14] and validates the two-cycle approach as an effective strategy for increasing ceramic precursor content in HIAM lattice structures.

After vacuum drying overnight at 60°C, both specimens showed a significant mass reduction (A-1: 0.6413 to 0.4269 g; A-2: 0.7431 to 0.3720 g), reflecting the removal of residual water from the hydrogel network and any unbound solution retained within the pores. Notably, the post-vacuum mass of specimen A-1 (0.4269 g) was slightly below its initial dry mass (0.4749 g), while A-2 (0.3720 g) finished further below its dry mass (0.4684 g), suggesting that the vacuum drying step removed not only free water but may have also caused partial loss of loosely bound precipitate. The net retained mass attributable to precipitated cerium hydroxide will be quantified by TGA.

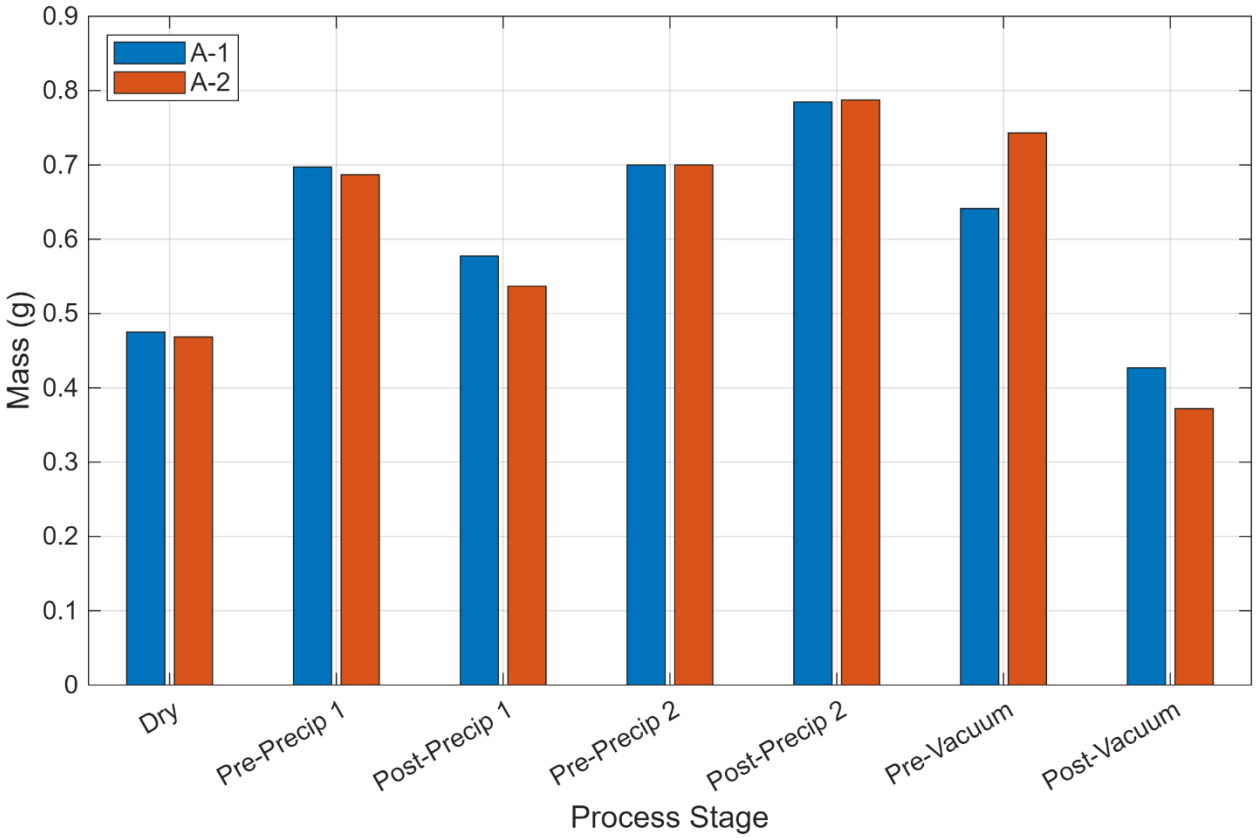

Figure 6-7: mass (g) at each process stage for A-1 and A-2

6.4 Calcination

Following the two-cycle infusion-precipitation protocol, the cerium-loaded gyroid lattice was subjected to the two-step thermal treatment described by Yee et al., consisting of debinding in nitrogen followed by sintering in air, both carried out at a maximum temperature of 1000°C. The heating profiles for each step are reproduced in Figure 6-8. This treatment was intended to remove the PEGDA/PEGMA polymer template and sinter the precipitated cerium hydroxide particles into a coherent ceramic network.

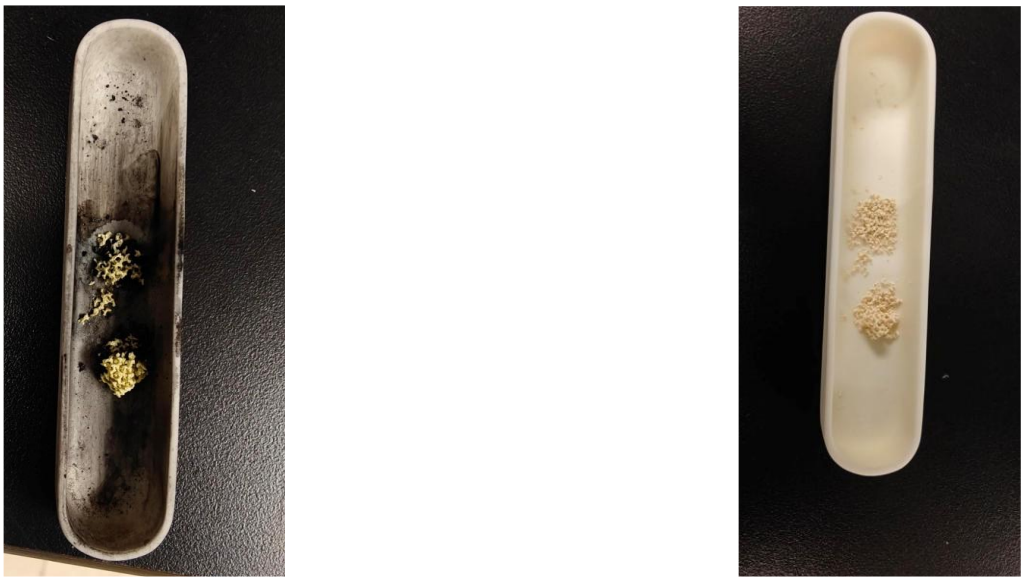

a) Gyroids.post.calcination *b) Gyroids.post.sintering*

Figure 6-8: Showing a) samples right out of furnace and b) failed samples as a result of transfer to clean crucible

Following thermal treatment, the structure was retrieved from the furnace visibly intact, with partial sintering evident from the consolidated appearance of the surface. However, the structure exhibited extreme mechanical fragility upon handling. During transfer from the furnace crucible to a secondary tray, the lattice fractured completely, leaving only fragments. Figure 6-8 shows the structure immediately after removal from the furnace and the resulting fragments following attempted transfer.

The failure is attributed to insufficient sintering temperature for the cerium hydroxide precursor system used in this study. The 1000°C protocol was developed by Yee et al [16]. for an iron oxide composite system; cerium oxide (CeO_2), the expected product of calcination of $Ce(OH)_3$ in

air, has a significantly higher sintering temperature than iron oxide, and 1000°C is unlikely to produce the neck formation and grain bonding necessary for structural cohesion in a ceria-based ceramic. The partial sintering visible on the surface suggests that some densification occurred at the outermost regions of the lattice where heat transfer was most direct, but the bulk of the structure remained insufficiently consolidated to survive mechanical handling. Higher sintering temperatures, in the range of 1300–1500°C typically reported for CeO_2 densification, will be required in subsequent work to produce a mechanically stable ceramic part from this precursor system.

6.5 Discussion

The results of this chapter demonstrate that HIAM fabrication of zirconia-based ceramic lattices using a PEGDA/PEGMA hydrogel resin and a $CeCl_3$ precursor solution is achievable in principle, though the process yield obtained on the Phrozen Sonic Mini 8K was low. The primary limitation was the bottom-up DLP architecture of the available printer, which generates a peel force at each layer that is incompatible with the mechanical fragility of high-water-content hydrogel green parts and the geometric complexity of the gyroid topology [52].The approximately 40 print attempts required to obtain two viable structures underscore this constraint. The use of increased bottom layer exposure time (75 s) and a gradual linear transition to body layer exposure (19 s over 12 transition layers) partially mitigated delamination but could not fully compensate for the inherent peel force of the bottom-up process.

The mass evolution data confirm that the two-cycle infusion-precipitation sequence successfully increased cerium loading relative to a single-cycle approach. The post-Precipitation Cycle 2 masses were substantially higher than post-Precipitation Cycle 1 masses for both specimens, consistent with the cumulative loading mechanism described by Yee et al [16]. The re-infusion step between cycles was critical to this outcome: without re-immersion in fresh solution, the second vapor exposure would act only on the ion population remaining after the first washing step, which was considerably reduced. The pre-Precipitation Cycle 2 mass of 0.7000 g for both specimens reflects the re-infused state and is comparable to or slightly above the pre-Precipitation Cycle 1 mass, confirming that the wash and re-infusion cycle effectively reloads the network.

The vacuum drying step introduced a notable mass reduction that varied between the two specimens. This variability may reflect differences in the degree of surface wetting or internal solution retention at the time of vacuum treatment, or partial loss of loosely bound precipitate during drying. TGA will be necessary to deconvolute the contribution of residual water from that of retained cerium hydroxide in the final dried mass. Until that analysis is complete, the net ceramic precursor content of the structures cannot be definitively quantified.

The sole use of $CeCl_3$ as the precursor in this chapter represents an intentional simplification relative to the ultimate goal of fabricating ceria-stabilized zirconia. A mixed-salt infusion using both $CeCl_3$ and $ZrOCl_2$ was not pursued because the infusion behavior of zirconium salt in combination with cerium salt has not yet been characterized in the HIAM context. The infusion study of Chapter 5 addressed each salt independently; their interaction within the hydrogel network under simultaneous infusion conditions, and the effect of that interaction on precipitation behavior, remains an open question. The present chapter therefore serves as a proof-of-concept demonstration using the better-characterized cerium system, with the mixed-salt case reserved for future work.

Taken together, the results establish that the PEGDA/PEGMA hydrogel formulation developed in Chapter 4 can reproduce the complex geometry of a gyroid minimal surface lattice, and that the two-cycle infusion-precipitation protocol produces measurable cumulative cerium loading in that geometry.

Chapter 7 Conclusions and Future Work

This chapter draws together the findings from Chapters 4 through 6, evaluates the extent to which the original objectives of the thesis were met, and identifies the limitations that constrain the conclusions. It then outlines a prioritized roadmap for future work that addresses the unresolved challenges in a logical sequence, from precipitation chemistry through to full ceramic characterization.

7.1 Summary of Results

This thesis set out to establish a viable HIAM process for the fabrication of ceria-stabilized zirconia ceramic lattices, with a specific focus on maximizing metal ion loading during the infusion stage to limit volumetric shrinkage. The work addressed three sequential objectives:

characterizing how resin composition affects hydrogel network properties, understanding the infusion behavior of Ce and Zr precursors, and demonstrating HIAM printing of CSZ lattice structures.

The parametric study in Chapter 4 demonstrated that both the PEGDA/PEGMA ratio and the initial water content exert significant independent effects on the equilibrium water content of the resulting hydrogel. Increasing PEGMA content disrupts crosslink regularity and increases mesh size, while higher initial water content promotes a more open, porous network architecture by acting as a porogen during photopolymerization. The formulation yielding the highest EWC of 71.70% (50/50 PEGDA/PEGMA at 30/70 polymer/water ratio under 10 s UV exposure) was identified as the theoretically optimal composition, though practical printing requirements led to the selection of the 50/50 polymer/water variant (Vial 8) as the working formulation.

The infusion experiments in Chapter 5 established that Ce^{3+} and Zr^{4+} exhibit meaningfully different uptake behaviors at equivalent bulk concentration. Ce^{3+} infuses progressively and achieves higher net mass uptake over extended infusion times, while Zr^{4+} approaches a lower equilibrium plateau more quickly, confirming that zirconium loading will be the limiting factor in a co-infusion protocol. Elevated temperature infusion accelerated kinetics but introduced geometric distortion incompatible with lattice fabrication requirements. Preliminary precipitation trials identified a critical unresolved challenge: the ammonium hydroxide precipitation approach displaced absorbed ions rather than fixing them, indicating that the precipitation chemistry requires fundamental re-examination before a complete multi-cycle HIAM process can be realized.

Chapter 6 demonstrated that gyroid lattice geometries can be printed from the Vial 8 formulation and advanced partway through the HIAM process sequence, confirming basic process compatibility. Two specimens were successfully printed and subjected to two infusion-precipitation cycles followed by vacuum drying, with mass measurements confirming cumulative cerium loading consistent with the Chapter 5 disc results. However, a notable limitation emerged during the post-precipitation handling stages: repeated infusion and precipitation cycles progressively embrittled the hydrogel scaffold, and both specimens sustained chips and minor fractures during transfer between processing vessels. This physical degradation is consistent with the progressive displacement of the water-swollen polymer network by cerium

hydroxide precipitate, which reduces the compliance and toughness of the hydrogel as the inorganic phase accumulates. The resulting fragility, combined with the consistently low print yields due to build plate adhesion failures, prevented full ceramic characterization within the scope of this study.

7.2 Implications

The findings of this thesis make several contributions to the development of HIAM as a platform for oxide ceramic fabrication, while acknowledging that the absence of a completed ceramic processing cycle limits the strength of some conclusions. The parametric resin study provides a quantitative framework for hydrogel network design that is directly applicable to other HIAM material systems beyond CSZ. The relationship between PEGDA/PEGMA ratio, water content, and equilibrium water fraction established here gives future practitioners a principled starting point for resin formulation, rather than relying on empirical trial and error. The identification of a printability threshold is a practically important design constraint that has not been explicitly quantified in prior HIAM literature for hydrogel systems of this composition. The infusion asymmetry between Ce^{3+} and Zr^{4+} identified in Chapter 5 is, to the best of the author's knowledge, the first direct experimental comparison of these two precursors within a HIAM hydrogel context. The finding that zirconium uptake saturates at a lower mass fraction and more quickly than cerium has concrete implications for co-infusion protocol design: it suggests that achieving the target Ce:Zr stoichiometry for Ce-TZP will require active management of relative ion concentrations, and that a simple equimolar co-infusion approach is unlikely to produce the intended composition without further optimization. The identification of ion displacement as the failure mode for ammonium hydroxide precipitation is a practically important finding that narrows the solution space for precipitation chemistry development. Rather than a parameter optimization problem like adjusting concentration, exposure time, or washing conditions, the result indicates that a fundamentally different precipitation mechanism is needed. This reframing is a meaningful contribution to the practical knowledge base for HIAM of multi-component oxide ceramics, even though it represents an unresolved challenge rather than a solved one. The demonstration in Chapter 6 that gyroid lattice structures can be printed from a PEGDA/PEGMA hydrogel resin and advanced through infusion and precipitation stages, despite the low yield and scaffold brittleness encountered, establishes a baseline for future process development. The mass uptake behavior of the lattice specimens was consistent with disc data from Chapter 5,

suggesting that the flat disc geometry used for parametric studies is a reasonable proxy for lattice infusion kinetics.

7.3 Challenges and Limitations

Several limitations constrain the conclusions that can be drawn from this study. The absence of a validated precipitation protocol is the most fundamental gap. Without a reliable method for fixing metal ions within the hydrogel network, the downstream process steps (multi-cycle loading, calcination, and sintering) could not be evaluated, and the ceramic yield and phase composition of the sintered product remain uncharacterized. All conclusions about HIAM process viability are therefore conditional on this challenge being resolved.

Scaffold brittleness during post-precipitation handling was a significant practical obstacle in Chapter 6. Both gyroid specimens sustained chips and minor fractures during transfer between processing vessels across the infusion-precipitation cycles, attributable to the progressive stiffening of the hydrogel as cerium hydroxide accumulated within the network. The narrow geometry of the processing vessels used in this study exacerbated handling difficulty; the use of wide-neck containers in future work would reduce the mechanical stress imposed on the specimen during transfer and is a straightforward mitigation. More broadly, the brittleness observation raises a question about the upper limit of ceramic loading that the hydrogel scaffold can accommodate before structural integrity is compromised, which has not yet been quantified.

The low print yield in Chapter 6, requiring approximately 40 attempts to obtain two viable specimens, prevented systematic evaluation of how process parameters affect final ceramic properties. The bottom-up DLP architecture of the Phrozen Sonic Mini 8K was identified as the primary driver of this yield loss, as the peel force generated at each layer separation exceeded the cohesive strength of the hydrogel green part. The intended solution, a top-down DLP printer, in which no peel force is generated, was not available during this study due to equipment delivery delays. This represents the most consequential equipment-related limitation of the work.

The infusion experiments were conducted on flat disc specimens rather than on printed lattice geometries. Diffusion path length effects in complex three-dimensional architectures, particularly in the gyroid where channel tortuosity may slow ion transport to interior regions, may produce different uptake distributions than those observed in discs. Until infusion experiments are conducted directly on lattice specimens across a range of unit cell sizes and wall

thicknesses, the transferability of the disc kinetic data to complex geometries remains an assumption rather than a confirmed result.

Finally, the co-infusion behavior of Ce and Zr when present simultaneously in solution has not yet been characterized. Competitive adsorption or complexation effects within the polymer network under co-infusion conditions may cause the actual Ce:Zr ratio in the infused scaffold to differ from what the single-salt experiments suggest, and this uncertainty propagates directly into the stoichiometry of the final ceramic.

7.4 Future Work

The results of this thesis define a clear and prioritized roadmap for advancing HIAM of CSZ toward a complete and reproducible process. The five areas below are ordered by dependency: each builds on the resolution of the one preceding it.

The most immediate priority is the development of a viable precipitation protocol. The failure of ammonium hydroxide precipitation to fix metal ions within the network indicates that the precipitation chemistry requires fundamental reconsideration rather than incremental adjustment. Several alternative approaches are worth evaluating systematically. Dilute sodium hydroxide addition at controlled rates offers precise pH management and may allow slower, more uniform hydroxide nucleation within the network. Urea-based homogeneous precipitation, in which urea hydrolysis generates hydroxide ions gradually throughout the solution, avoids the steep concentration gradients associated with direct base addition and has precedent in ceramic powder synthesis.

Citric acid chelation to pre-stabilize Zr^{4+} prior to pH adjustment is a further candidate, particularly relevant given the tendency of zirconium to hydrolyze prematurely at moderate pH [53].

The key criterion for evaluating any candidate protocol is the retention of precipitated material within the hydrogel network after the precipitant is removed, which can be assessed gravimetrically by comparing disc mass before and after a wash step. This screening approach allows rapid evaluation of multiple chemistries before committing to lattice-scale trials.

Second, print process reliability must be improved before lattice characterization becomes meaningful. The transition to a top-down DLP configuration is the highest-leverage change

available: by eliminating the peel force entirely, it addresses the root cause of the ~40-attempt yield loss observed in Chapter 6 and should substantially improve the reproducibility of lattice fabrication. In parallel, build plate adhesion under the bottom-up architecture can be further optimized through surface treatment of the build plate, adjustment of the bottom layer count and exposure time, or the use of a sacrificial adhesion layer as an interim measure. The scaffold fragility observed under the Vial 8 formulation, including the chips and fractures sustained during transfer between processing vessels, suggests that a slightly higher polymer fraction or a brief additional UV post-cure step may improve mechanical integrity without substantially reducing ion uptake capacity. Handling protocols should also be revised: the use of wide-neck processing containers would reduce the bending and torsional loads imposed on the specimen during transfer and is a low-cost mitigation that can be implemented immediately.

Third, once a reliable precipitation protocol is established, multi-cycle infusion-precipitation experiments should be conducted on disc specimens to quantify how ceramic yield and linear shrinkage evolve with cycle number. This directly addresses the central challenge of CSZ HIAM identified in Chapter 2 and will establish the minimum number of cycles required to reach a target ceramic mass fraction sufficient for a coherent sintered part. Dimensional measurements at each cycle will provide an early indicator of shrinkage behavior without requiring full thermal processing.

Fourth, co-infusion experiments using mixed Ce-Zr solutions should be conducted to characterize whether the two ions compete for network uptake sites and whether the Ce:Zr ratio in the infused scaffold matches the target stoichiometry for Ce-TZP. The single-salt infusion asymmetry identified in Chapter 5 suggests that equimolar co-infusion solutions will not yield the intended 10-12 mol% CeO_2 stabilizer content without compensatory adjustments to the solution composition. EDS or ICP-OES analysis of the dried precipitate will allow the actual Ce:Zr ratio to be quantified and compared to the target stoichiometry.

If competitive uptake is confirmed, strategies such as sequential infusion or adjustment of the Ce:Zr molar ratio in the infusion solution may be used to achieve the desired scaffold composition [54].

Finally, once full ceramic processing is achieved through calcination and sintering, XRD characterization should be used to confirm the presence and fraction of the tetragonal zirconia

phase stabilized by cerium, and SEM-EDS should be used to assess compositional homogeneity at the microstructural level. Dimensional measurements of the sintered lattice relative to the green part will quantify total linear shrinkage and allow comparison to the shrinkage values reported for other HIAM ceramic systems. These measurements will collectively determine whether the HIAM process as developed here produces a Ce-TZP ceramic with the phase constitution, microstructural homogeneity, and geometric fidelity required for structural and functional performance.

Chapter 8 References

[1] D. Godec *et al.*, "Introduction to Additive Manufacturing," in *A Guide to Additive Manufacturing*, D. Godec, J. Gonzalez-Gutierrez, A. Nordin, E. Pei, and J. Ureña Alcázar, Eds., in Springer Tracts in Additive Manufacturing. , Cham: Springer International Publishing, 2022, pp. 1–44. doi: 10.1007/978-3-031-05863-9_1.

[2] W. E. Frazier, "Metal Additive Manufacturing: A Review," *J. Mater. Eng. Perform.*, vol. 23, no. 6, pp. 1917–1928, Jun. 2014, doi: 10.1007/s11665-014-0958-z.

[3] A. Mostafaei *et al.*, "Binder jet 3D printing—Process parameters, materials, properties, modeling, and challenges," *Prog. Mater. Sci.*, vol. 119, p. 100707, Jun. 2021, doi: 10.1016/j.pmatsci.2020.100707.

[4] I. Gibson, D. Rosen, and B. Stucker, *Additive Manufacturing Technologies: 3D Printing, Rapid Prototyping, and Direct Digital Manufacturing*. New York, NY: Springer New York, 2015. doi: 10.1007/978-1-4939-2113-3.

[5] W. Du, X. Ren, Z. Pei, and C. Ma, "Ceramic Binder Jetting Additive Manufacturing: A Literature Review on Density," *J. Manuf. Sci. Eng.*, vol. 142, no. 4, p. 040801, Apr. 2020, doi: 10.1115/1.4046248.

[6] J. Gonzalez-Gutierrez, S. Cano, S. Schuschnigg, C. Kukla, J. Sapkota, and C. Holzer, "Additive Manufacturing of Metallic and Ceramic Components by the Material Extrusion of Highly-Filled Polymers: A Review and Future Perspectives," *Materials*, vol. 11, no. 5, p. 840, May 2018, doi: 10.3390/ma11050840.

[7] J. W. Halloran, "Ceramic Stereolithography: Additive Manufacturing for Ceramics by Photopolymerization," *Annu. Rev. Mater. Res.*, vol. 46, no. 1, pp. 19–40, Jul. 2016, doi: 10.1146/annurev-matsci-070115-031841.

[8] X. Wang, F. Schmidt, D. Hanaor, P. H. Kamm, S. Li, and A. Gurlo, "Additive manufacturing of ceramics from preceramic polymers: A versatile stereolithographic approach assisted by thiol-ene click chemistry," *Addit. Manuf.*, vol. 27, pp. 80–90, May 2019, doi: 10.1016/j.addma.2019.02.012.

[9] B. Derby, "Inkjet Printing of Functional and Structural Materials: Fluid Property Requirements, Feature Stability, and Resolution," *Annu. Rev. Mater. Res.*, vol. 40, no. 1, pp. 395–414, Jun. 2010, doi: 10.1146/annurev-matsci-070909-104502.

[10] B. Derby, "Inkjet printing ceramics: From drops to solid," *J. Eur. Ceram. Soc.*, vol. 31, no. 14, pp. 2543–2550, Nov. 2011, doi: 10.1016/j.jeurceramsoc.2011.01.016.

[11] E. Feilden, E. G.-T. Blanca, F. Giuliani, E. Saiz, and L. Vandeperre, "Robocasting of structural ceramic parts with hydrogel inks," *J. Eur. Ceram. Soc.*, vol. 36, no. 10, pp. 2525–2533, Aug. 2016, doi: 10.1016/j.jeurceramsoc.2016.03.001.

[12] Y. Lakhdar, C. Tuck, J. Binner, A. Terry, and R. Goodridge, "Additive manufacturing of advanced ceramic materials," *Prog. Mater. Sci.*, vol. 116, p. 100736, Feb. 2021, doi: 10.1016/j.pmatsci.2020.100736.

[13] M. A. Saccone, R. A. Gallivan, K. Narita, D. W. Yee, and J. R. Greer, "Additive manufacturing of micro-architected metals via hydrogel infusion," *Nature*, vol. 612, no. 7941, pp. 685–690, Dec. 2022, doi: 10.1038/s41586-022-05433-2.

[14] D. W. Yee, M. L. Lifson, B. W. Edwards, and J. R. Greer, "Additive Manufacturing of 3D-Architected Multifunctional Metal Oxides," *Adv. Mater.*, vol. 31, no. 33, p. 1901345, 2019, doi: 10.1002/adma.201901345.

[15] D. W. Yee, M. A. Citrin, Z. W. Taylor, M. A. Saccone, V. L. Tovmasyan, and J. R. Greer, "Hydrogel-Based Additive Manufacturing of Lithium Cobalt Oxide," *Adv. Mater. Technol.*, vol. 6, no. 2, p. 2000791, Feb. 2021, doi: 10.1002/admt.202000791.
[16] Y. Ji and D. Yee, "Low Shrinkage Hydrogel Infusion Additive Manufacturing of Ceramics and Metals," Apr. 16, 2025. doi: 10.26434/chemrxiv-2025-vwjgv.
[17] S. Fournier *et al.*, "Ceria-stabilized zirconia-based composites printed by stereolithography: Impact of the processing method on the ductile behaviour and its transformation features," *J. Eur. Ceram. Soc.*, vol. 43, no. 7, pp. 2894–2906, Jul. 2023, doi: 10.1016/j.jeurceramsoc.2022.11.006.
[18] W. Samociuk, E. Hevorkian, T. Prikhna, V. Chishkala, A. Mamalis, and M. Rucki, "Peculiarities of Yttria- and Ceria-Stabilized Zirconia Ceramics Fabricated via Electroconsolidation," *Materials*, vol. 19, no. 4, p. 776, Feb. 2026, doi: 10.3390/ma19040776.
[19] M. Yarahmadi, G. Fargas Ribas, and J. J. Roa Rovira, "3D printing of zirconia-based ceramic materials," Universitat Politècnica de Catalunya, 2023. doi: 10.5821/dissertation-2117-400821.
[20] H. Zhang and S. LeBlanc, "Processing Parameters for Selective Laser Sintering or Melting of Oxide Ceramics," in *Additive Manufacturing of High-performance Metals and Alloys - Modeling and Optimization*, I. V. Shishkovsky, Ed., InTech, 2018. doi: 10.5772/intechopen.75832.
[21] H. Shao *et al.*, "3D Printing of Bioceramic Multifunctional Scaffolds for Bone Tissue Engineering," *Adv. Funct. Mater.*, vol. 35, no. 49, p. e09039, 2025, doi: 10.1002/adfm.202509039.
[22] A. Du Plessis, "Effects of process parameters on porosity in laser powder bed fusion revealed by X-ray tomography," *Addit. Manuf.*, vol. 30, p. 100871, Dec. 2019, doi: 10.1016/j.addma.2019.100871.
[23] H. A. Soliman, J. Pineault, and M. Elbestawi, "Influence of Combined Heat Treatment and Hot Isostatic Pressure (HT-HIP) on Titanium Aluminide Processed by L-PBF," *Materials*, vol. 16, no. 14, p. 5071, Jul. 2023, doi: 10.3390/ma16145071.
[24] C. Wu *et al.*, "Multi-physics modeling of side roughness generation mechanisms in powder bed fusion," *Addit. Manuf.*, vol. 47, p. 102274, Nov. 2021, doi: 10.1016/j.addma.2021.102274.
[25] D. Gailevičius, V. Padolskytė, L. Mikoliūnaitė, S. Šakirzanovas, S. Juodkazis, and M. Malinauskas, "Additive-manufacturing of 3D glass-ceramics down to nanoscale resolution," *Nanoscale Horiz.*, vol. 4, no. 3, pp. 647–651, 2019, doi: 10.1039/C8NH00293B.
[26] X. Yu *et al.*, "Microstructure formation mechanisms and property regulation methods during ceramic additive manufacturing," *J. Manuf. Process.*, vol. 131, pp. 1548–1564, Dec. 2024, doi: 10.1016/j.jmapro.2024.09.112.
[27] S. K. Paral, D.-Z. Lin, Y.-L. Cheng, S.-C. Lin, and J.-Y. Jeng, "A Review of Critical Issues in High-Speed Vat Photopolymerization," *Polymers*, vol. 15, no. 12, p. 2716, Jun. 2023, doi: 10.3390/polym15122716.
[28] D. J. Whyte, E. H. Doeven, A. Sutti, A. Z. Kouzani, and S. D. Adams, "Volumetric additive manufacturing: A new frontier in layer-less 3D printing," *Addit. Manuf.*, vol. 84, p. 104094, Mar. 2024, doi: 10.1016/j.addma.2024.104094.

[29] L. Goyos-Ball *et al.*, “The effects of laser patterning 10CeTZP-Al2O3 nanocomposite disc surfaces: Osseous differentiation and cellular arrangement in vitro,” *Ceram. Int.*, vol. 44, no. 8, pp. 9472–9478, Jun. 2018, doi: 10.1016/j.ceramint.2018.02.164.
[30] A. K. Nikumbh and P. V. Adhyapak, “Formation characterization and rheological properties of zirconia and ceria-stabilized zirconia,” *Nat. Sci.*, vol. 02, no. 07, pp. 694–706, 2010, doi: 10.4236/ns.2010.27086.
[31] R. Wang, C. Cheng, H. Wang, and D. Wang, “Swollen hydrogel nanotechnology: Advanced applications of the rudimentary swelling properties of hydrogels,” *ChemPhysMater*, vol. 3, no. 4, pp. 357–375, Oct. 2024, doi: 10.1016/j.chphma.2024.07.006.
[32] J. Xia *et al.*, “Regulation of cell attachment, spreading, and migration by hydrogel substrates with independently tunable mesh size,” *Acta Biomater.*, vol. 141, pp. 178–189, Mar. 2022, doi: 10.1016/j.actbio.2022.01.025.
[33] K. Zhang, K. Wang, J. Chen, K. Wei, B. Liang, and R. He, “Design and additive manufacturing of 3D-architected ceramic metamaterials with programmable thermal expansion,” *Addit. Manuf.*, vol. 47, p. 102338, Nov. 2021, doi: 10.1016/j.addma.2021.102338.
[34] T. T. Tran, R. A. Gallivan, and J. R. Greer, “Multiscale Microstructural and Mechanical Characterization of Cu-Ni Binary Alloys Reduced During Hydrogel Infusion-Based Additive Manufacturing (HIAM),” *Small*, vol. 21, no. 36, Sep. 2025, doi: 10.1002/smll.202501320.
[35] N. S. Yaw *et al.*, “Precursor design for additive manufacturing of ceramics through hydrogel infusion,” *Inorg. Chem. Front.*, vol. 12, no. 8, Apr. 2025, doi: 10.1039/d5qi00139k.
[36] Y. Garanin, R. Shakirziyanov, D. Borgekov, N. Volodina, D. Shlimas, and M. Zdorovets, “Influence of precursors and mineralizers on phase formation in ZrO2 nanoparticles synthesized by the hydrothermal method,” *Sci. Rep.*, vol. 15, p. 26165, Jul. 2025, doi: 10.1038/s41598-025-12213-1.
[37] R. Xu *et al.*, “A new approach for impregnation of Cs into zirconia microsphere matrix,” *Ceram. Int.*, vol. 49, no. 17, Part A, pp. 27780–27787, Sep. 2023, doi: 10.1016/j.ceramint.2023.05.251.
[38] S. M. Yakout and H. S. Hassan, “Adsorption Characteristics of Sol Gel-Derived Zirconia for Cesium Ions from Aqueous Solutions,” *Molecules*, vol. 19, no. 7, pp. 9160–9172, Jul. 2014, doi: 10.3390/molecules19079160.
[39] J. A. Beamish, J. Zhu, K. Kottke-Marchant, and R. E. Marchant, “The effects of monoacrylated poly(ethylene glycol) on the properties of poly(ethylene glycol) diacrylate hydrogels used for tissue engineering,” *J. Biomed. Mater. Res. A*, vol. 92A, no. 2, pp. 441–450, Feb. 2010, doi: 10.1002/jbm.a.32353.
[40] M. Levin, Y. Tang, C. D. Eisenbach, M. T. Valentine, and N. Cohen, “Understanding the Response of Poly(ethylene glycol) diacrylate (PEGDA) Hydrogel Networks: A Statistical Mechanics-Based Framework,” *Macromolecules*, vol. 57, no. 15, pp. 7074–7086, Aug. 2024, doi: 10.1021/acs.macromol.3c02635.
[41] N. Kladovasilakis, K. Tsongas, D. Karalekas, and D. Tzetzis, “Architected Materials for Additive Manufacturing: A Comprehensive Review,” *Materials*, vol. 15, no. 17, p. 5919, Aug. 2022, doi: 10.3390/ma15175919.
[42] Z. Schoe *et al.*, “Fabrication of a Zircon Microfiltration Membrane for Culture Medium Sterilization,” *Membranes*, vol. 13, no. 4, p. 399, Mar. 2023, doi: 10.3390/membranes13040399.
[43] A. H. Schoen, “Infinite Periodic Minimal Surfaces Without Self-Intersections,” 1970.

[44] O. Al-Ketan, R. Rowshan, and R. K. Abu Al-Rub, “Topology-mechanical property relationship of 3D printed strut, skeletal, and sheet based periodic metallic cellular materials,” *Addit. Manuf.*, vol. 19, pp. 167–183, Jan. 2018, doi: 10.1016/j.addma.2017.12.006.
[45] D. W. Abueidda, M. Elhebeary, C.-S. (Andrew) Shiang, S. Pang, R. K. Abu Al-Rub, and I. M. Jasiuk, “Mechanical properties of 3D printed polymeric Gyroid cellular structures: Experimental and finite element study,” *Mater. Des.*, vol. 165, p. 107597, Mar. 2019, doi: 10.1016/j.matdes.2019.107597.
[46] I. Roohani, E. Newsom, and H. Zreiqat, “High-resolution vat-photopolymerization of personalized bioceramic implants: new advances, regulatory hurdles, and key recommendations,” *Int. Mater. Rev.*, vol. 68, no. 8, pp. 1075–1097, Nov. 2023, doi: 10.1080/09506608.2023.2194744.
[47] G. M. Cruise, D. S. Scharp, and J. A. Hubbell, “Characterization of permeability and network structure of interfacially photopolymerized poly(ethylene glycol) diacrylate hydrogels,” *Biomaterials*, vol. 19, no. 14, pp. 1287–1294, Jul. 1998, doi: 10.1016/S0142-9612(98)00025-8.
[48] X. Li *et al.*, “Insight into the limitation of the Beer–Lambert law in stereolithography ceramic 3D printing: a study on irradiance parameters and slurry curing,” *Virtual Phys. Prototyp.*, vol. 20, no. 1, p. e2544761, Dec. 2025, doi: 10.1080/17452759.2025.2544761.
[49] F. Della Sala, M. Biondi, D. Guarnieri, A. Borzacchiello, L. Ambrosio, and L. Mayol, “Mechanical behavior of bioactive poly(ethylene glycol) diacrylate matrices for biomedical application,” *J. Mech. Behav. Biomed. Mater.*, vol. 110, p. 103885, Oct. 2020, doi: 10.1016/j.jmbbm.2020.103885.
[50] T. Jiang *et al.*, “Study of Forming Performance and Characterization of DLP 3D Printed Parts,” *Materials*, vol. 16, no. 10, p. 3847, May 2023, doi: 10.3390/ma16103847.
[51] S. Subedi, S. Liu, W. Wang, S. M. A. Naser Shovon, X. Chen, and H. O. T. Ware, “Multi-material vat photopolymerization 3D printing: a review of mechanisms and applications,” *Npj Adv. Manuf.*, vol. 1, no. 1, p. 9, Nov. 2024, doi: 10.1038/s44334-024-00005-w.
[52] F. Liravi, S. Das, and C. Zhou, “Separation force analysis and prediction based on cohesive element model for constrained-surface Stereolithography processes,” *Comput.-Aided Des.*, vol. 69, pp. 134–142, Dec. 2015, doi: 10.1016/j.cad.2015.05.002.
[53] F. Kazemi, F. Arianpour, M. Taheri, A. Saberi, and H. R. Rezaie, “Effects of chelating agents on the sol-gel synthesis of nano-zirconia: Comparison of the Pechini and sugar-based methods,” *Int. J. Miner. Metall. Mater.*, vol. 27, no. 5, pp. 693–702, May 2020, doi: 10.1007/s12613-019-1933-3.
[54] P. Khajavi *et al.*, “Tetragonal phase stability maps of ceria-yttria co-doped zirconia: From powders to sintered ceramics,” *Ceram. Int.*, vol. 46, no. 7, pp. 9396–9405, May 2020, doi: 10.1016/j.ceramint.2019.12.199.